Thermodynamics of oiling-out in antisolvent crystallization. I. Extrapolation of ternary phase diagram from solubility to instability

Zhengyu Zhang, Ran Bi, Jean-Frédéric Audibert, Weixi Wang, Soo Young Park, Anne Spasojevic - de Biré, Robert Bernard Pansu

To cite this version:

Zhengyu Zhang, Ran Bi, Jean-Frédéric Audibert, Weixi Wang, Soo Young Park, et al.. Thermodynamics of oiling-out in antisolvent crystallization. I. Extrapolation of ternary phase diagram from solubility to instability. Crystal Growth & Design, 2023, 24 (1), pp.224-237. 10.1021/acs.cgd.3c00916 . hal-04373603

HAL Id: hal-04373603
https://centralesupelec.hal.science/hal-04373603

Submitted on 5 Jan 2024

Thermodynamics of oiling-out in antisolvent crystallization. I. Extrapolation of ternary phase diagram from solubility to instability

Zhengyu Zhang[1,2,3*], Ran Bi[4], Jean-Frédéric Audibert[3,4], Weixi Wang[5], Soo Young Park[6], Anne Spasojevic-de Biré[1], Robert Bernard Pansu[2,3]

[1] Université Paris-Saclay, CentraleSupélec, CNRS, Laboratoire SPMS, 91190 Gif-sur-Yvette, France
[2] Université Paris-Saclay, CNRS, Ecole Normale Supérieure Paris-Saclay, CentraleSupélec, Laboratoire LuMIn, 91190 Gif-sur-Yvette, France
[3] Université Paris Saclay, Institut d'Alembert (IDA), CNRS, Ecole Normale Supérieure Paris-Saclay, 91190 Gif-sur-Yvette, France
[4] Université Paris-Saclay, CNRS, Ecole Normale Supérieure Paris-Saclay, Laboratoire PPSM, 91190 Gif-sur-Yvette, France
[5] École polytechnique, LPICM, CNRS, Institut Polytechnique de Paris, 91120 Palaiseau, France
[6] Department of Materials Science and Engineering, Seoul National University, 1 Gwanak-ro, Gwanak-gu, Seoul 151-744, Korea

*Correspond to: zhengyu.zhang@centralesupelec.fr

Keywords

Anti-solvent crystallization; Phase diagram calculation; Microfluidics; Oiling-out; Polymorphism; Anti-solvent focusing

Abstract

The competition between crystallization and oiling-out is a major concern in the process design of antisolvent crystallization for poorly water-soluble drugs. Within the CALPHAD framework, this study demonstrates the extrapolation of the ternary phase diagram for antisolvent crystallization from the solubility data, resorting to the Jouyban-Acree model and the Gibbs–Helmholtz type equation. The ternary phase diagram for DBDCS (a fluorophore exhibiting aggregation-induced emission) in water-[1,4-dioxane] is constructed by calculating the polymorph solid-liquid equilibria, the metastable liquid-liquid equilibrium, and the spinodal limit. Our computational results agree with the phase diagram measured through microfluidics. By analyzing the chemical potential, we show that the solute uphill diffusion relies on the antisolvent gradient. The energy of disorder upon nucleation is found to be much smaller compared to the solute energy gain upon antisolvent addition. The characteristics of the parallel solubility curves of the polymorphs are explained with the analysis of the molecular interactions. By evaluating the energy of composition fluctuation, we suggest the optimal conditions for antisolvent crystallization. The insights obtained from this study can be extended to the process design of antisolvent crystallization for similar systems, and form the basis for further kinetic analysis of the competition between oiling-out and crystallization.

1 Introduction

Practically water-insoluble (< 0.1 mg/mL) chemicals have been estimated to make up ~70% of the new drugs in development and ~40% of the drugs established.[1] The need for improving their bioavailability, though in competition with the stability, has spurred extensive research into more soluble phases, cocrystals, and dispersed morphologies.[2, 3] While the surface-to-volume ratio[4, 5] is an important factor, it is the polymorphism[6, 7] that substantially determines the stability, the crystal habit, the solubility, and the dissolution rate. The stable polymorph is favored by thermodynamics, yet intermediate pathways can be more viable due to kinetics. Should the supersaturation exceed the thermodynamic instability limit, even spinodal decomposition can be triggered.

The Liquid Anti-Solvent (LAS) process is a convenient separation technique for controlling solvent composition and solute supersaturation, with applications such as screening polymorphs[8-10], preparing micro-/nano-particles[11-13], and microfluidics[14-17]. Liquid-Liquid Phase Separation (LLPS)[18-21] has been observed prior to Anti-Solvent Crystallization (ASC) at high supersaturations. It is dubbed "oiling-out"[22], given that the intermediate phase is typically an organic liquid emerging from an aqueous solution where solid crystals are expected. This phenomenon has attracted theoretical interest, as the highly concentrated amorphous intermediates are considered to play a pivotal role in non-classical nucleation mechanisms[23-26]. LLPS in ASC is a manifestation of Anti-Solvent Precipitation (ASP), yet with the continuous (solute-lean) and the dispersed (solute-rich) phase both being metastable compared to the crystalline phase. Subsequent solidification or crystallization kinetically facilitates the formation of nano-/micro-powders from the dispersed phase while hindering the formation of high-quality crystals from the continuous phase.

Strategies to avoid or utilize LLPS in ASC remain largely empirical. External interventions to mitigate (*e.g.* by seeding[27-29] or ultrasound[30, 31]) or to induce (*e.g.* by electric field[32, 33] or laser[34, 35]) LLPS have been explored. However, the most pertinent and practicable methodology is to design procedures based on phase diagrams. In contrast to compilations of ternary phase diagrams of metallic systems, a handful of experimentally determined polythermal ternary phase diagrams[19, 22, 36-43] addressing LLPS in ASC can be found in the literature. Thermodynamic calculation[44-49] offers an alternative approach, reducing the number of experimental measurements needed. The physics and mathematics underlying phase diagram calculation remain challenging and captivating, one and a half centuries since the pioneering work of Gibbs[50] and decades following those of Meijering[51, 52] and Cahn[53-55].

The CALPHAD (CALculation of PHAse Diagrams) approach predicts phase equilibria and stability by extrapolating thermodynamic data from binary subsystems to higher-order systems.[56] A prerequisite is the thermodynamic description of the constituent binary systems. In the case of ASC, the Vapor-Liquid Equilibrium (VLE) of the cosolvent binary mixture is usually previously investigated, yet the thermodynamic data on the two solute-solvent binary subsystems are rarely available. The solubility of poorly water-soluble organic drugs in aqueous-organic cosolvent mixtures is described by the Jouyban-Acree (J-A) equation[57-59], which is mathematically derived[59, 60] from a 2-Body and 3-Body (2B3B) interactional mixing model[61]. The correlation between the low solubility and the 2B3B parameters allows for the extraction of the thermodynamic parameters of solute-solvent subsystems from solubility data. The 2B3B model describes the mixing of liquids; knowing the relative Gibbs energy of the solute polymorphs allows for predicting the polymorph solubilities. This energy can be assessed from Differential Scanning Calorimetry (DSC) data.

To address the challenge of LLPS in ASC, this study demonstrates the thermodynamic calculation of the ternary phase diagram for a poorly water-soluble organic solute in aqueous-organic cosolvents. The example solute, DBDCS ((2Z,2'Z)-2,2'-(1,4-phenylene)bis(3-(4-butoxyphenyl) acrylonitrile), **Figure 1**), has been previously investigated in a microfluidic system[14, 62]. It is insoluble in water (the non-solvent) but slightly soluble in 1,4-dioxane (the "good" solvent). Its fluorescence depends on the molecular arrangement[63, 64], enabling further *in situ* characterization of the polymorphism and the phase transitions. Two polymorphs of DBDCS have been reported[64]: the γ phase (green emission, fluorescence lifetime > 10 ns) and the β phase (blue emission, fluorescence lifetime < 6 ns). We calculate the chemical potentials, the phase instability, the spinodal decomposition limit, the metastable Liquid-Liquid Equilibrium (LLE) binodal, and the polymorph Solid-Liquid Equilibria (SLE), based on a minimum number of experimental measurements. The input experimental data include the solute solubility data as a function of solvent composition, the DSC data of the solute polymorphs up to the melting temperature, and the VLE data of the binary mixture of the cosolvents. The thermodynamic models are introduced in Section 2; the thermodynamic parameter optimization is the subject of Section 3; the CALPHAD methodology is described in Section 4; the *in silico* phase diagram is presented in Section 5; the computation is validated with the microfluidic phase diagram in Section 6; finally in Section 7, the crystallization process design, the solute uphill diffusion, the two-step crystallization, and the molecular interactions are discussed by analyzing the Gibbs energies on the phase diagram. This methodology can be extended to the process design of ASC for other poorly water-soluble organic solutes. We hope that our contribution will serve as the basis for further thermodynamic and kinetic analysis of the competition between oiling-out and crystallization.

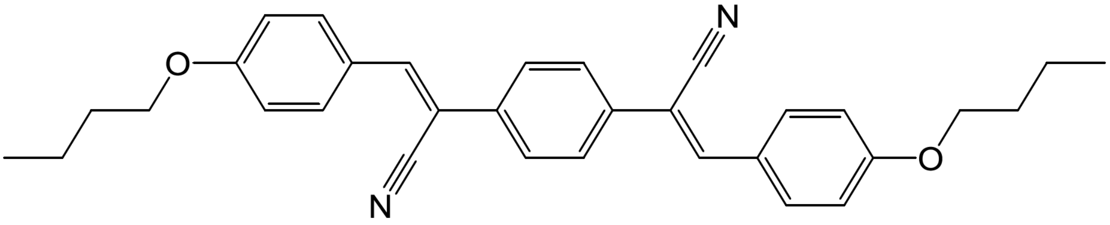

Figure 1. Molecular structure of DBDCS ((2Z,2'Z)-2,2'-(1,4-phenylene)bis(3-(4-butoxyphenyl) acrylonitrile)). Formula: $C_{32}H_{32}N_2O_2$; Molecular mass: 476.60.

2 Thermodynamic models

2.1 Two-Body and three-Body interactional mixing model

The 2B3B model[59-61] describes the excess Gibbs energy of mixing, $G_{\mathrm{m}}^{\mathrm{EX}}$, by counting the probabilities of the 2-body and the 3-body binary molecular interactions. Neglecting the excess volume and the excess entropy, the 2B3B model expresses the excess molar Gibbs energy of mixing for a binary liquid mixture *i-j* as[61]:

$$G_{ij,\mathrm{m}}^{\mathrm{EX}} = x_i x_j \left(\Omega_{ij} + a_{ij} {x_i}^3 + b_{ij} {x_j}^3 \right), \tag{1}$$

where x_i denotes the amount fraction of component i, and Ω_{ij}, a_{ij} and b_{ij} are the adjustable parameters. The symmetric Ω_{ij} is interpreted as the binary interaction energy, similar to that in the regular solution model, *cf.* Section S.1 of the Supporting Information. The two additional parameters describe the asymmetry of the binary interaction, a_{ij} being interpreted as related to the degree of self-clustering of component *i* in the *i-j* interaction, and b_{ij} that of component *j*.

The 2B3B parameters are optimized for each binary system and held for the extrapolation to higher-order systems. The excess Gibbs energy in a ternary system *i-j-k* has been shown mathematically[61] to be the summation of the constituent binary expressions:

$$G_{ijk,\mathrm{m}}^{\mathrm{EX}} = G_{ij,\mathrm{m}}^{\mathrm{EX}} + G_{ik,\mathrm{m}}^{\mathrm{EX}} + G_{jk,\mathrm{m}}^{\mathrm{EX}} \ . \tag{2}$$

The excess chemical potential of component i in mixture *i-j-k* is:

$$\begin{aligned} \mu_i^{\mathrm{EX}} = (1 - x_i)\left[x_j \left(\Omega_{ij} + 4a_{ij} {x_i}^3 \right) + x_k (\Omega_{ik} + 4a_{ik} {x_i}^3) \right] + (1 - 4x_i) \\ \left(b_{ij} {x_j}^4 + b_{ik} {x_k}^4 \right) - x_j x_k \left(\Omega_{jk} + 4a_{jk} {x_j}^3 + 4b_{jk} {x_k}^3 \right) \ . \end{aligned} \tag{3}$$

The 2B3B model has been tested with the VLE data of simple ternary aqueous-organic liquid mixtures, such as [1,4-dioxane]-ethanol-water, acetone-ethanol-water, and acetonitrile-ethanol-water, and with the LLE data of water-ethanol-benzene.[61] The J-A equation, describing the SLE in ASC, is derived from the 2B3B model.[59, 60]

2.2 Jouyban-Acree equation for low solubility in aqueous-organic cosolvents

The log-linear relation is an attempt to describe the solubility of poorly soluble solutes in aqueous-organic cosolvent mixtures at constant temperature and pressure[65]:

$$\ln s = \phi_1^0 \ln s_1 + \phi_2^0 \ln s_2 \ , \tag{4}$$

with s the solubility in the mixture, s_i the solubility in neat solvent i, and ϕ_i^0 the solute-free volume fraction of solvent i.

Jouyban and Acree have shown that the deviation of the actual solubility from the log-linear Equation (4) can be described by a second-order Redlich-Kister type polynomial in terms of the solvent volume fractions[59, 60]:

$$\ln s = \phi_1^0 \ln s_1 + \phi_2^0 \ln s_2 + \frac{\phi_1^0 \phi_2^0}{T} \sum_{n=0}^{2} A_n (\phi_2^0 - \phi_1^0)^n , \tag{5}$$

with T the temperature and A_n the adjustable parameters.

The J-A parameters are optimized for each pair of aqueous-organic cosolvents and have been reported to be insensitive to the specific organic solutes[66-70]. This brings convenience as the optimized parameters can be used to predict the solubilities of similar poorly soluble solutes in the same cosolvent system. The solubility prediction with the J-A equation has been validated for more than fifty drugs in water-[1,4-dioxane] mixture at various temperatures[69-73], as well as for some other over one hundred water-[organic solvent]-drug systems[57, 58, 66-68, 70, 72, 74-78]. The solubility predictions for proteins[79, 80] and electrolytes[81] in cosolvents have also be proposed.

3 Thermodynamic parameter optimization

3.1 From solubility data in solvent mixture

The J-A equation is derived—in its amount-fraction representation, termed as the "Combined Nearly Ideal Binary Solvent/Redlich-Kister (CNIBS/R-K) expression"[59, 60]—from the 2B3B model. Acree and Jouyban have correlated the parameters of the CNIBS/R-K expression to the "interaction energies" of the ternary 2B3B model:

$$\begin{aligned} \ln x_{3\mathrm{s}} &= x_1^0 \ln x_{3\mathrm{s}1} + x_2^0 \ln x_{3\mathrm{s}2} + \frac{x_1^0 x_2^0}{RT} \sum_{n=0}^{3} B_n (x_2^0 - x_1^0)^n \\ &= x_1^0 \ln x_{3\mathrm{s}1} + x_2^0 \ln x_{3\mathrm{s}2} + \frac{x_1^0 x_2^0}{RT} \left(P_0 + P_1 x_2^0 + P_2 {x_2^0}^2 + P_3 {x_2^0}^3 \right), \end{aligned} \tag{6}$$

$$\begin{aligned}
P_0 &= B_0 - B_1 + B_2 - B_3 = \Omega_{12} + 4a_{12} + a_{23} + 3a_{13} ,\\
P_1 &= 2B_1 - 4B_2 + 6B_3 = -12a_{12} + a_{23} - 3a_{13} ,\\
P_2 &= 4B_2 - 12B_3 = 12a_{12} + a_{23} + a_{13} ,\\
P_3 &= 8B_3 = -4a_{12} + 4b_{12} ,\\
&(x_{3\mathrm{s}}, x_{3\mathrm{s}1}, x_{3\mathrm{s}2} \ll 1) ,
\end{aligned}$$

where the non-solvent is component 1, the good solvent is component 2, and the solute is component 3, $x_{3\mathrm{s}}$ denotes the amount-fraction solubility, $x_{3\mathrm{s}i}$ is the amount-fraction solubility in solvent i, x_i^0 indicates the solute-free amount fraction of solvent i, R is the ideal gas constant, B_n and P_n are the adjustable parameters, and Ω_{ij}, a_{ij}, and b_{ij} the "interaction energies" in the 2B3B model.

In the present work, we investigate water (component 1)-[1,4-dioxane] (component 2)-DBDCS (component 3) at $T_\mathrm{r} \equiv 298.15$ K. The parameters for 1-2 interaction, $\Omega_{12} \approx 1.7RT_\mathrm{r}$, $a_{12} \approx -0.14RT_\mathrm{r}$, and $b_{12} \approx 0.37RT_\mathrm{r}$, were optimized by fitting the VLE data[82, 83] (Section S.2) of water (1)-[1,4-dioxane] (2) binary system to the binary 2B3B Equation (1). We have measured the solubility (Section S.3) of the γ phase of DBDCS (3) in water (1)-[1,4-dioxane] (2) mixture at T_r. The unknown parameters in Equation (6) were thus fitted from the solubility data, giving $a_{23} \approx -1.9RT_\mathrm{r}$ and $a_{13} \approx 20RT_\mathrm{r}$.

3.2 From DSC data

The 2B3B model describes the energy of liquid mixing; knowing the Gibbs energy differences between the solute polymorphs and its metastable liquid allows for the prediction of the polymorph SLE:

$$RT\ln x_{3\mathrm{s}} + \mu_3^{\mathrm{EX}} = G_{3(\mathrm{S}),\mathrm{m}}(T) - G_{3(\mathrm{L}),\mathrm{m}}(T) = -\Delta_{\mathrm{S}\to\mathrm{L}}G_{3,\mathrm{m}}(T) , \tag{7}$$

where the left-hand side is the chemical potential of the solute (3) relative to its liquid state, μ_3^{EX} is given in Equation (3), and $G_{3(\mathrm{S}),\mathrm{m}} - G_{3(\mathrm{L}),\mathrm{m}}$ denotes the molar Gibbs energy of the solute in solid (S) relative to the liquid phase (L), which is the opposite of its molar Gibbs energy of fusion, $\Delta_{\mathrm{S}\to\mathrm{L}}G_{3,\mathrm{m}}$. The assessment of $\Delta_{\mathrm{S}\to\mathrm{L}}G_{3,\mathrm{m}}(T)$ at undercooled temperatures can be done by integrating the Gibbs-Helmholtz equation,

$$\left(\frac{\partial\left(\frac{\Delta G}{T}\right)}{\partial T}\right)_p = -\frac{\Delta H}{T^2}\,, \tag{8}$$

from the melting temperature down to the temperature of interest, where G denotes Gibbs energy, p is pressure, and H is enthalpy.

With the DSC data[64] of the polymorphs of DBDCS (3), we used (detail *cf.* Section S.4) Turnbull's[84] formula (S6) to assess $\Delta_{\gamma\rightarrow\beta}G_{3,\mathrm{m}}(T) \approx 1.1RT_\mathrm{r}$, between the two polymorphs, and Hoffman's[85] equation (S7) to assess $\Delta_{\beta\rightarrow\mathrm{L}}G_{3,\mathrm{m}}(T) \approx 2.5RT_\mathrm{r}$, between the β phase and the metastable liquid. Their sum gives $\Delta_{\gamma\rightarrow\mathrm{L}}G_{3,\mathrm{m}}(T) \approx 3.6RT_\mathrm{r}$, between the γ phase and the metastable liquid.

3.3 From solubility data in neat solvents

Given that the solubility $x_{3\mathrm{s}} \ll 1$, substitution of Equation (3) into Equation (7) for the γ SLE in neat solvent *i* brings[60]:

$$-\Delta_{\gamma\rightarrow\mathrm{L}}G_{3,\mathrm{m}}(T) = RT\ln x_{3si} + \Omega_{i3} + a_{i3}\,, \quad (x_{3si} \ll 1). \tag{9}$$

With the values of $\Delta_{\gamma\rightarrow\mathrm{L}}G_{3,\mathrm{m}}(T)$ and a_{i3} known from previous steps, Equation (9) gave $\Omega_{13} \approx 3.9RT_\mathrm{r}$ and $\Omega_{13} \approx 6.0RT_\mathrm{r}$ from the solubilities in neat solvent 1 and 2, respectively.

The exact values of the thermodynamic parameters used in the phase diagram calculation are listed in Section S.5. The values of b_{13} and b_{23} could be extracted by measuring the saturated concentrations of the solvents in the undercooled liquid solute (3). Such self-clustering of the solute (3) is only apparent at its high concentrations, as b_{13} and b_{23} are empirically fitted to the third-power of x_3. They are not important in our simulation.

4 CALPHAD method

The CALPHAD method extrapolates binary interaction functions and parameters into higher-order systems, usually without optimization of higher-order terms unless experimentally proven necessary.[56] Liquid and disordered solid systems are most commonly described by regular solution type models. The 2B3B model is essentially a third-order regular solution type model, *cf.* Section S.1. The 2B3B model may not be superior than other higher-order regular solution type models, but its correlation with the J-A model allows for the optimization of the thermodynamic parameters from the low solubility. With the parameters optimized in the previous steps, we assessed the chemical potential of each component, the Gibbs energy of the mixture, and their derivatives in terms of composition.

Knowing the Gibbs energies as a function of composition allows for the calculation of phase equilibria and stability. Gibbs[50] established the necessary and sufficient conditions of phase equilibria: the chemical potential of each component (along with the temperature and pressure) being equal in each phase, as defined in Section S.6. In this study, the LLPS limit is defined by the equilibrium between two ternary liquid mixtures, *cf.* Equation $(\mathrm{S}8)$. These are the double tangent point pairs of the *G-x* (Gibbs energy, G, as a function of composition in amount fraction, x) surface. The polymorph solubilities are defined by the equilibria between the polymorphs of DBDCS (3) and the ternary solution, *cf.* Equation (7). This is the intersection of the energy level of the polymorph with the chemical potential of the solute in the solution. Gibbs[50, 53] further demonstrated the necessary and sufficient conditions of internal thermodynamic stability of a homogeneous multicomponent system: the chemical potential of each component increasing with its amount of substance, *cf.* Section S.7. The spinodal decomposition limit is defined by the Hessian determinant of the molar Gibbs energy, $|\mathbf{H}(G_\mathrm{m})|$, being zero, *cf.* Equation $(\mathrm{S}10)$. This is where the *G-x* surface changes its concave-convexity. A C++ Newton-Raphson iterative algorithm was used to calculate the numerical solutions of the spinodal limit, the metastable LLE, and the polymorph SLE.

5 Computational results

5.1 Ternary phase diagram of water-[1,4-dioxane]-DBDCS at 298.15 K

5.1.1 A generic shape

The Gibbs energy of mixing for water (1)-[1,4-dioxane] (2)-DBDCS (3) ternary system at 1 atm and 298.15 K is shown in **Figure 2**. The calculated spinodal curves (in red), metastable LLE binodal curves (cyan), and SLE curves (only discernable in **Figure 2**B) of the β phase (blue) and the γ phase (green) are plotted. The phase diagram is partitioned into the spinodal decomposition region, the LLPS region, the crystallization region, and the dissolution region.

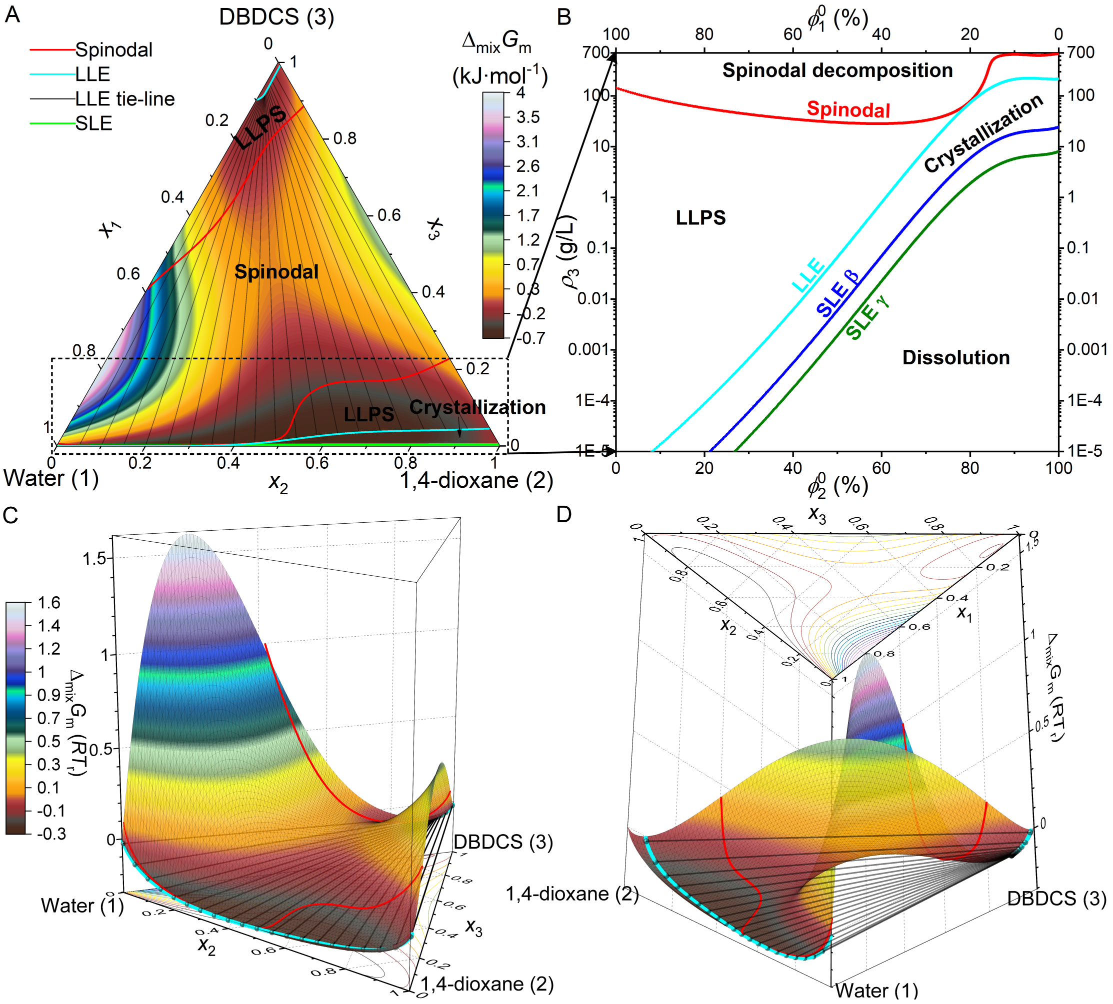

Figure 2. Assessment of the molar Gibbs energy of mixing, $\Delta_{mix}G_m$, relative to the liquid reference states, for the ternary mixture of water (1)-[1,4-dioxane] (2)-DBDCS (3) at 298.15 K. A: $\Delta_{mix}G_m$ plotted on the Gibbs triangle in terms of amount fraction composition

x; B: detailed view of the low concentration part, plotted in terms of the solute mass concentration, ρ_3, against the solute-free solvent volume fractions, ϕ_2^0 and ϕ_1^0; C: side view of the G-x surface; D: oblique bottom view of the G-x surface. The phase diagram is partitioned into the spinodal decomposition region, the LLPS region, the crystallization region, and the dissolution region. $RT_\mathrm{r} \approx 2.5\mathrm{kJ} \cdot \mathrm{mol}^{-1}$.

Figure 2 represents a generic shape of the ternary phase diagram for ASC of poorly water-soluble organic solutes. It is characterized by a simple band-like[52] structure, with all the curves meandering through the Gibbs triangle and intersecting the solute-solvent binary edges. The majority of the G-x surface is on a saddle. The full miscibility of water (1)-[1,4-dioxane] (2) is shown by $\Delta_\mathrm{mix}G_\mathrm{m}$ being convex on the entire 1-2 edge. The limited solubility of DBDCS (3) in 1,4-dioxane (2) is the result of the concavity on the 2-3 edge. The insolubility is even more pronounced in water (1), as evidenced by a higher peak on the 1-3 edge. Detailed descriptions of three binary subsystems can be found in Section S.8. To demonstrate the LLE pairs, a set of exemplary tie-lines are plotted in black. They are the double tangent points of the G-x surface, as seen in **Figure 2**D. On the solute-rich side, the LLE curve squishes close to vertex 3, indicating that the oiling-out is not the pure liquid solute but with solvent contaminants, which can be purified after its crystallization. This is reflected by the fact that crystals obtained through oiling-out are often contaminated by impurities. On the solvent-rich side, the LLE and the SLE curves stretch above the 1-2 edge, exhibiting parallelism on the logarithmic scale, as seen in **Figure 2**B.

It is noteworthy that the 1-3 concavity (height $\sim 1.6RT_\mathrm{r}$) is higher than the 2-3 concavity (height $\sim 0.4RT_\mathrm{r}$), despite the binary interaction energy Ω_{13} $(\sim 3RT_\mathrm{r})$ being smaller than Ω_{23} $(\sim 5RT_\mathrm{r})$. This discrepancy can be attributed to the asymmetry in the molecular interactions, with a_{13} $(\sim 20RT_\mathrm{r})$ being significantly larger than a_{23} $(\sim -2RT_\mathrm{r})$, which still yields a higher peak on the 1-3 edge and makes water (1) the antisolvent. Water is infamous for exhibiting concentration dependent hydrogen-bonding network structures.[86]

5.1.2 Instability and spinodal curves

In **Figure 2**, the red spinodal curves indicate where the *G*-*x* surface changes from concave-convex to full convex. This is defined by the Hessian determinant of the molar Gibbs energy, $|\mathbf{H}(G_\mathrm{m})|$, as plotted in **Figure 3**. The Hessian matrix $\mathbf{H}(G_\mathrm{m})$ describes the local concave-convexity of a surface: the surface is convex in the direction with a positive eigenvalue and concave in the direction with a negative eigenvalue, *cf.* Section S.7. Between the two spinodal curves, the *G*-*x* surface is concave-convex with $|\mathbf{H}(G_\mathrm{m})| < 0$. Along a concave direction of the *G*-*x* surface, an infinitesimal composition fluctuation (*cf.* Equation (S13)) will result in a reduction of the Gibbs energy, leading to amplification and spread of spinodal decomposition. Outside the two red curves, the *G*-*x* surface is strictly convex with $|\mathbf{H}(G_\mathrm{m})| > 0$. There, an infinitesimal composition fluctuation in any direction causes an increase in the Gibbs energy, and therefore a phase transition needs to initiate through a nucleation event.

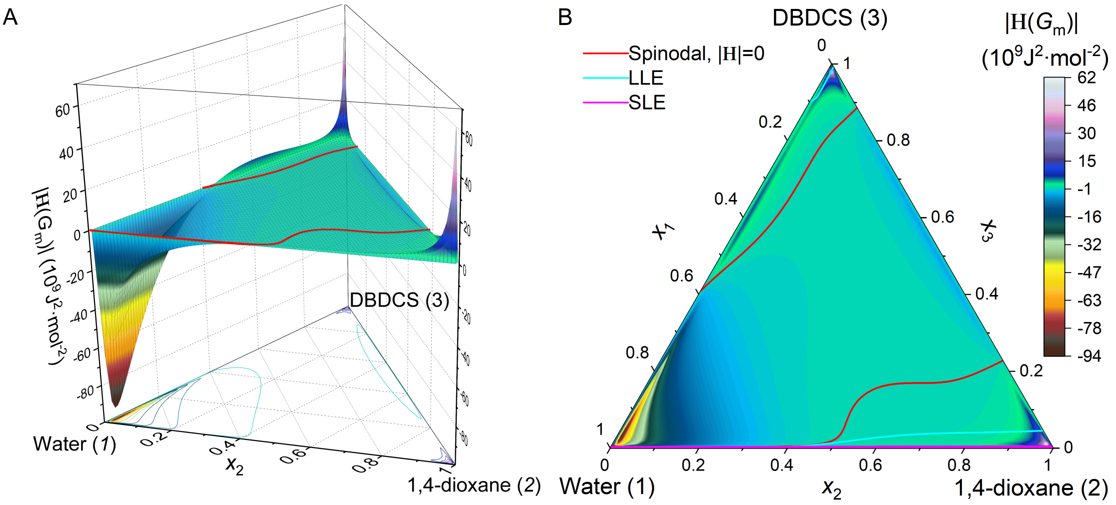

Figure 3. Assessment of the Hessian determinant, $|\mathbf{H}(G_\mathrm{m})|$, of the molar Gibbs energy of water (1)-[1,4-dioxane] (2)-DBDCS (3) at 298.15 K, plotted in terms of amount fraction composition *x*. A: side view; B: top view. The spinodal decomposition limit (red curves) is the intersection of $|\mathbf{H}(G_\mathrm{m})|$ with zero. A homogenous mixture is instable between the two spinodal curves, where $|\mathbf{H}(G_\mathrm{m})| < 0$.

Figure 3 shows that the liquid mixture is highly stable near the vertices of dioxane (2) where $x_2 > \sim 0.85$ and of DBDCS (3) where $x_3 > \sim 0.95$, indicated by the two peaks of

$|\mathbf{H}(G_\mathrm{m})|$. However, away of those regions, $|\mathbf{H}(G_\mathrm{m})|$ abruptly drops to negative values close to zero for the majority part of the triangle, rendering the system instable. Within a relatively large triangle close to the vertex of water (1) where $x_1 > \sim 0.6$, $|\mathbf{H}(G_\mathrm{m})|$ undergoes another significant descent, signifying the extreme instability.

LAS processes are performed in the solvent rich part. There, x_3 on the spinodal curve is minuscule within the range of $x_2 < \sim 0.4$. It ascends drastically around $x_2 \approx 0.5$ ($\phi_2^0 \approx 80\%$), reaching a plateau of $x_3 \approx 0.2$. ($\sim 700\ \mathrm{g \cdot L^{-1}}$). The presence of the abrupt rise persists even when nullifying the a_{ij} and b_{ij} terms of the 2B3B model. It depends mainly on the value of the binary interaction energy Ω_{12} between the two solvents. A value of $\Omega_{12} < 1.5RT_\mathrm{r}$ would eliminate the bend, while a value of $\Omega_{12} > 2RT_\mathrm{r}$ would lead to a miscibility gap between the two solvents and a fall of the ternary spinodal curve. The actual value of Ω_{12} is $\sim 1.7RT_\mathrm{r}$, indicating a weak repulsion between water (1)-[1,4-dioxane] (2) that is just slightly over-powered by the entropy of mixing. This rise of the spinodal curve at $x_2 \approx 0.5$ is a reminder of the close-to-instability nature of water (1)-[1,4-dioxane] (2) mixture and might be specific to this pair of cosolvents.

5.1.3 Chemical potentials and phase equilibria

The chemical potential of each component relative to the liquid state is plotted in **Figure 4**, with the same tie-lines from **Figure 2**. The tie-lines are horizontal on each of the μ-x (chemical potential, μ, as a function of amount fraction, x) surfaces, indicating that each component in every double tangent pair possesses equal chemical potential. The polymorph SLE are determined by the intersections of the chemical potentials of the crystals ($\sim -2.5RT_\mathrm{r}$ for the γ phase and $\sim -3.6RT_\mathrm{r}$ for the β phase, relative to the liquid state) on the μ_3-x surface, as shown in **Figure 4**C.

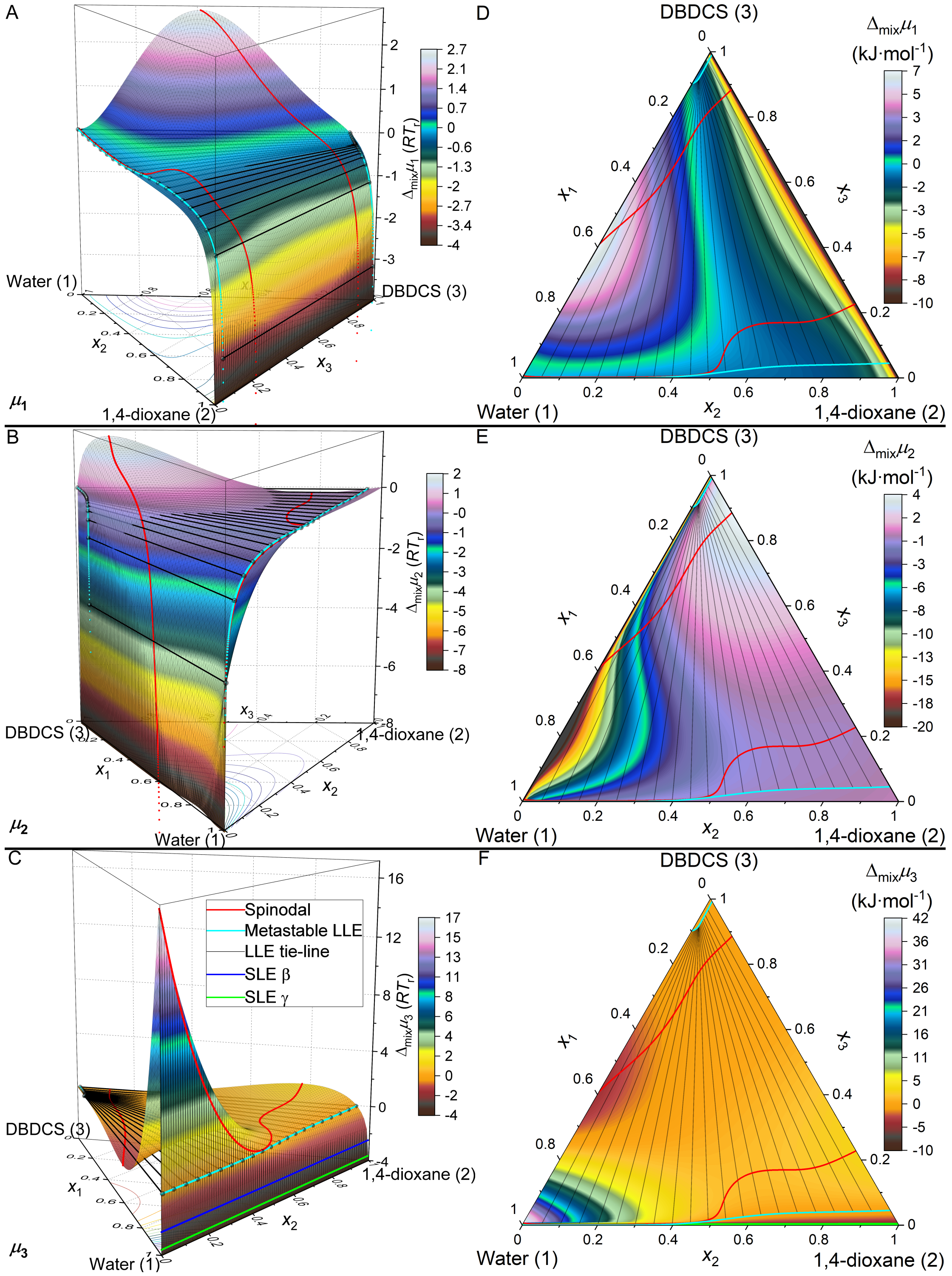

Figure 4. Assessment of the chemical potential μ for each component of water (1)-[1,4-dioxane] (2)-DBDCS (3) at 298.15 K, plotted in terms of amount fraction composition x. A, B, C are side views of μ_1, μ_2, and μ_3, respectively, and D, E, F the top views. The $\Delta_{\text{mix}}\mu_i$ denotes the chemical potential of component i relative to the liquid state. A set of LLE tie-

lines are plotted on the μ-x surfaces. The polymorph SLE are the intersections of the chemical potentials of the polymorphs on the μ_3-x surface. $RT_\mathrm{r} \approx 2.5\mathrm{kJ} \cdot \mathrm{mol}^{-1}$.

The undulations of μ at elevated concentrations are the result of the interplay among the interactions of the three subsystems. In **Figure 4**A, the very low affinity between water (1) and DBDCS (3) gives an uplift on the μ_1-x surface with the maximum locates close to the middle of the 1-3 edge where $x_1 \approx 0.59$ with $\mu_1 \approx 2.7RT_\mathrm{r}$. The 1-3 system in this work is significantly asymmetric, characterized by a large $a_{13} \approx 20RT_\mathrm{r}$ but $b_{13} = 0$; otherwise, the hump would have moved closer to vertex 3. In **Figure 4**B, the relatively weaker interaction between 1,4-dioxane (2) and DBDCS (3) brings a lower hump on the μ_2-x surface near the 2-3 edge. Since the 2-3 system is more symmetric, the top of the μ_2-x hump sits close to vertex 3 at $x_2 \approx 0.11$ with $\mu_2 \approx 1.6RT_\mathrm{r}$. The maxima of the μ_1-x and the μ_2-x surfaces correspond the two ends of the spinodal curve on the solute-rich side, where the concave-convexity of the G-x surface changes. In **Figure 4**C, the strong 1-3 repulsion leads to a high summit on the μ_3-x surface on the 1-3 edge at $x_3 \approx 0.006$ with $\mu_3 \approx 17RT_\mathrm{r}$, and the relatively low 2-3 repulsion results in a small hump on the 2-3 edge at $x_3 \approx 0.23$ with $\mu_3 \approx 1.3RT_\mathrm{r}$. The maxima of the μ_3-x surface coincide with the two ends of the spinodal curve in the solvent-rich part.

These μ-x maps are essential for understanding systems involved in mass exchange. We focus on the behavior of the solute. It is the entropy dominated sheer precipice of μ_3-x that determines the antisolvent focusing effect (Section 7.2), the solute energy gain upon antisolvent addition (Section 7.3), and the characteristics of the solubility curves (Section 7.4). The undulations dominated by molecular interactions govern spinodal decomposition. The first derivatives of the μ-x determine the direction and magnitude of diffusion fluxes. Accessing μ for all components forms the foundation for further multicomponent diffusion simulations.

6 Microfluidic phase diagram

Microfluidics enables *in situ* observation and precise control of mixing conditions while utilizing a minimal amount of solute. We used a coaxial microfluidic mixer[14, 62] to measure the phase diagram for the ASC of water (1)-[1,4-dioxane] (2)-DBDCS (3), the results plotted in **Figure 5**. The microfluidic phase diagram exhibits satisfactory agreement with the thermodynamic calculations: interdiffusion without phase transition were observed mainly in the dissolution region, crystallization in the crystallization region, and amorphous precipitation in the LLPS region. Note that the crystals were only recorded in the upper-right region of the crystallization region, slightly away from the good solvent (2). The calculation of the polymorph solubilities suggests that the points above the β SLE have higher probabilities to be the β phase, and those below to be the γ phase. On the left side of the crystallization region, the mixing easily goes into LLPS, as the distance between the LLE and SLE curves decreases exponentially with the fraction of the 1,4-dioxane (2). The points of amorphous precipitation below the LLE are transient observations depended on the mixing conditions away from equilibrium, which will be addressed in Section 7.2.

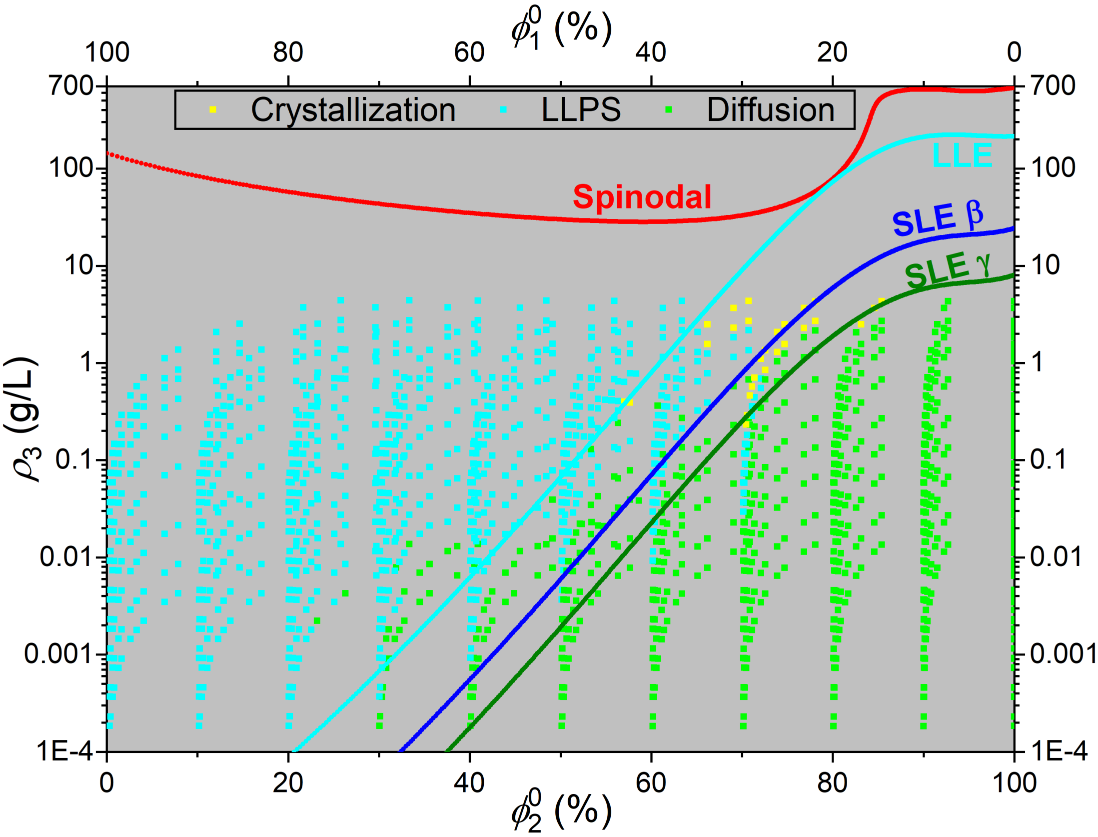

Figure 5. Microfluidic phase diagram of DBDCS (3) in water (1)-[1,4-dioxane] (2) at 298.15 K, plotted in terms of the solute mass concentration, ρ_3, against the solute-free solvent

volume fractions, ϕ_2^0 and ϕ_1^0. The curves are the thermodynamic predictions. The color-coded discrete points represent the types of observation, plotted on the average composition of the mixture: cyan for amorphous precipitation, yellow for crystallization, and green for interdiffusion without phase transition. Crystallization and amorphous precipitation were distinguished through *in situ* birefringence. The transient phase transitions were followed for typically less than 10 seconds along the microfluidic channel after the mixing nozzle.

7 Discussion

7.1 Crystallization process design from the Hessian surface

The energy gain of a composition fluctuation $\delta\mathbf{x}$ can be evaluated, through the second-order Taylor expansion of the Gibbs energy, as $\delta\mathbf{x}^{\mathrm{T}} \cdot \mathbf{H}(G_{\mathrm{m}}) \cdot \delta\mathbf{x}$ (*cf.* Section S.7). In the spinodal decomposition region, if $|\mathbf{H}(G_{\mathrm{m}})|$ approaches zero, the composition fluctuation barely reduces energy, and thus spinodal decomposition be more difficult.[53] In reverse, outside the spinodal decomposition region, the smaller the $|\mathbf{H}(G_{\mathrm{m}})|$, the lower resistance of the system to perturbations. The $|\mathbf{H}(G_{\mathrm{m}})|$ of water (1)-[1,4-dioxane] (2)-DBDCS (3) at $298.15\ \mathrm{K}$ is presented in **Figure 6** as the color map. It indicates that nucleation from the supersaturated solute in the "good" solvent is not easy.

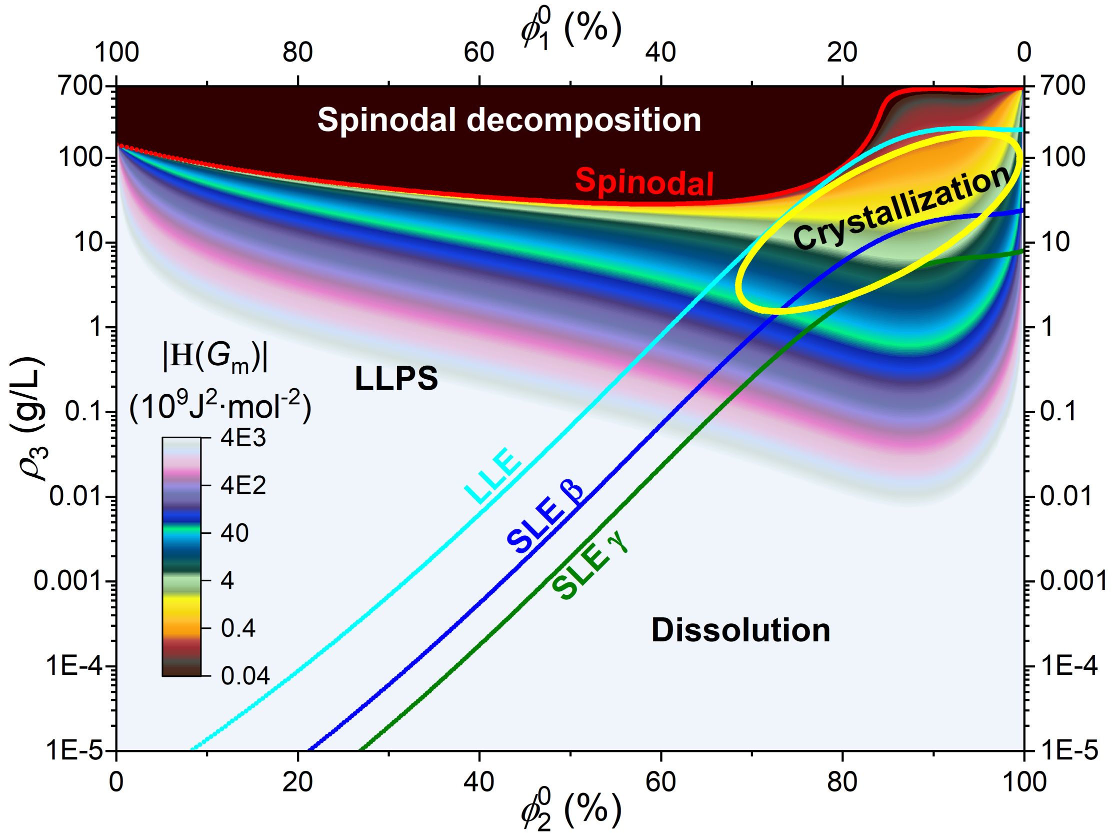

Figure 6. Optimal conditions, indicated by the yellow oval, for the antisolvent crystallization of water (1)-[1,4-dioxane] (2)-DBDCS (3) at 298.15 K, plotted on the phase diagram in terms of the solute mass concentration, ρ_3, against the solute-free solvent volume fractions, ϕ_2^0 and ϕ_1^0. The Hessian determinant, $|\mathbf{H}(G_\mathrm{m})|$, of the Gibbs energy is presented as the color map. The resistance to perturbations is assessed to be orders of magnitudes smaller within the yellow oval compared to the rest of the crystallization region.

To promote crystallization, **Figure 6** suggests the optimal conditions for ASC to be within the yellow oval, where the energy gain of an infinitesimal composition fluctuation is evaluated to be orders of magnitudes smaller compared to the rest of the crystallization region, providing a much more favorable environment for nucleation. Considering the dissolution upon antisolvent addition and the level of supersaturation, the practical conditions should be about the lower-left corner of the yellow oval. Furthermore, the polymorph SLE predict that conditions above the β SLE have higher probabilities to produce the β phase.

To avoid oiling-out, the composition needs to stay below the LLPS limit. However, on the one hand, in the range of $\phi_2^0 < \sim 60\%$ $(x_2 < \sim 0.25)$, the offset between the LLE and SLE is assessed to be smaller than $1\ \mathrm{g/L}$, such that LLPS will be difficult to avoid. On the other hand, real mixing is under dynamic mass exchange, not the homogeneous conditions of **Figure 6**. Even with the compositions before and after the mixing precisely chosen between the SLE and the metastable LLE curves, the diffusion trajectories can still enter the LLPS region. This is where the simulation of multicomponent diffusion becomes important.

To promote LLPS, the process design should be near the neat antisolvent (1), as both the LLE curve itself and the distance between the LLE and SLE curves decrease exponentially with ϕ_2^0. However, the spinodal decomposition limits on both water-rich and dioxane-rich sides require extremely high supersaturation ratios. Therefore, the most likely condition for observing spinodal decomposition is suggested to be in the intermediate range around $\phi_2^0 \approx 60\%$ $(x_2 \approx 0.24)$, as indicated by the minimum of the spinodal limit.

7.2 Antisolvent focusing seen from the chemical potential surface

It has been observed[62] in the microfluidic ASC that the solute is concentrated, towards the volume with a higher fraction of the "good" solvent, by the incoming antisolvent diffusion, leading to a focused precipitation. We have coined this phenomenon "antisolvent focusing". In **Figure 7**, μ_3 is plotted as a color map on the phase diagram. Three hypothetical diffusion couples, **L-H1** (meaning two solutions of compositions **L** and **H1** in contact), **L-H2**, and **L-H3** are given. These three diffusion couples have the same solute concentration gradient but different antisolvent gradients. In **L-H1**, solute molecules will diffuse "down" from **H1** (high ρ_3) to **L** (low ρ_3). Conversely, in **L-H3**, the solute migration direction is "up" from **L** (low ρ_3 but high μ_3) to **H3** (high ρ_3 but low μ_3). This is because energy, not concentration, gradient is the driving force for molecular migration. The limit of the antisolvent focusing effect is the μ_3-x contours, to which **L-H2** is parallel. In **L-H2**, the solute molecular tends to be stagnant. It is noteworthy to emphasize the generality of the antisolvent focusing effect: first, this is not in the domain of phase instability, and second, the three diffusion couples can be positioned together anywhere below the spinodal curve without altering the conclusion.

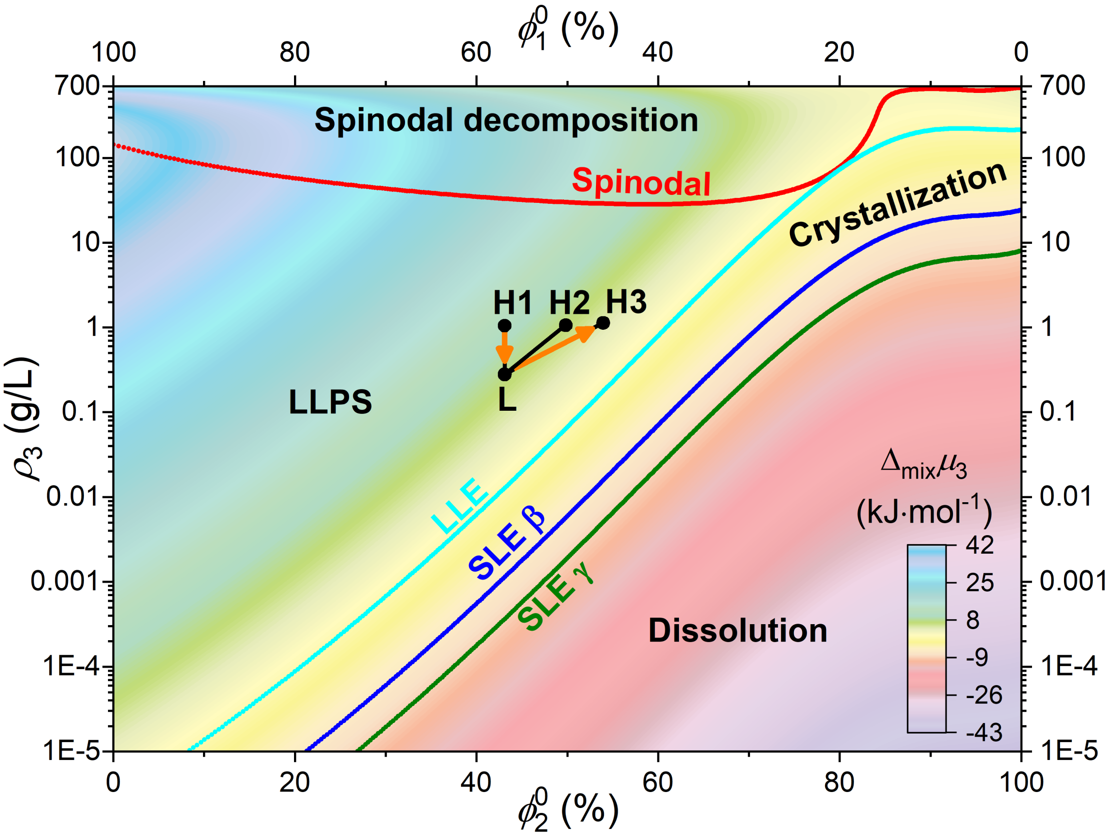

Figure 7. Diffusion directions of DBDCS (3) in hypothetical diffusion couples plotted on the phase diagram of water (1)-[1,4-dioxane] (2)- DBDCS (3) at 298.15 K in terms of the solute mass concentration, ρ_3, against the solute-free solvent volume fractions, ϕ_2^0 and ϕ_1^0. The color map represents $\Delta_{mix}\mu_3$, the chemical potential of DBDCS (3) relative to the liquid state. Three example diffusion couples, **L-H1** (meaning two solutions of compositions **L** and **H1** in contact), **L-H2**, and **L-H3**, are presented. The migration directions of DBDCS (3) molecules are indicated by the arrows. The contours of μ_3-x give the limit of the antisolvent gradient for the focusing effect, as in **L-H2**. The solubility curves also follow the contours of μ_3-x at the specific polymorph energy levels.

Figure 7 reveals that the antisolvent focusing effect depends on the scale and the magnitude of the gradient of antisolvent. During the solvent mixing, as soon as the composition gradient becomes parallel to the μ_3-x contours, the antisolvent focusing effect will diminish, unless a phase transition has already been triggered under the high supersaturation. This is why the rates of antisolvent addition and agitation affect the particle size and why the Ouzo-effect[87] is a common occurrence in LAS processes. The antisolvent focusing is responsible for the transient precipitations observed below the LLE in **Figure 5**.

7.3 Phase transitions seen from the chemical potential surface

7.3.1 Oiling-out: two-step crystallization

Diffusional phase transitions reduce the Gibbs energy of the system through composition, structure, and energy fluctuations. In the case of spinodal decomposition, thermodynamic forces amplify and spread composition fluctuations towards separation thanks to the concave directions of the *G*-*x* surface. The composition of the fluctuation will continuously evolve over the Gibbs triangle, until some equilibrium be established. The first equilibrium outside the spinodal decomposition region is the metastable LLE binodal.

But for a phase transition to initiate from a homogeneous phase outside the spinodal region, the nucleation theory considers a fluctuation large in degree but small in extent, which may survive if the decrease in its volume Gibbs energy compensates the increase in its surface energy. Despite the most stable crystalline phase, the nucleation of intermediate phases can be faster. If the parent solution is in the LLPS region, droplet nuclei can continue growing until the metastable LLE is established.

Following LLPS in ASC, crystals can nucleate from both the solute-rich droplets and the solvent-rich continuous phase. Experiments show that the crystals obtained after oiling-out are typically small and less pure.[19, 29] To obtain high quality crystals, nucleation from the continuous phase is preferred. However, nucleation from the nearly pure liquid solute is a much smaller composition fluctuation compared to that from the solvent-rich phase. Further, the interfacial energy between the solute liquid and the solute crystal is expected to be smaller compare to that between the solvent-rich phase and the crystal. For such kinetic factors, crystal nucleation from the dispersed phase is more efficient than from the continuous phase. Once some droplets have crystallized, they act as seeds, attracting solute molecules from the supersaturated continuous phase, thereby further hindering the slow crystallization of bigger, high-quality gems from the solution. To wit, in a metastable homogenous mixture between the spinodal limit and the LLPS limit, droplets are favored over crystals; following the droplet precipitation, crystals from the droplets are favored over those from the solution. This is a two-step crystallization through LLPS.

7.3.2 Two-step nucleation

The two-step nucleation, birth of a crystal through an amorphous cluster, has been proposed to be more efficient than the classical nucleation and has been observed under extreme conditions.[26] This is a giant fluctuation in both composition and energy. The liquid solute is less stable compared to the crystals, rendering this reaction path unlikely. We see that the energy cost of the two-step nucleation with respect of the classical nucleation corresponds to the Gibbs energy of fusion. In the case of DBDCS (3), the energy difference between its metastable liquid and crystals is $\sim 2.5RT_\mathrm{r}$ for the γ phase and $\sim 3.6RT_\mathrm{r}$ for the β phase at 298.15 K. Whereas **Figure 4**C shows that, upon the addition of water (1), the local μ_3 rises up to $\sim 41\ \mathrm{kJ/mol} \approx 17RT_\mathrm{r}$. The energy required to form the liquid nucleus is much smaller compared to what is provided by the antisolvent process. This makes the formation of metastable phases much easier compared to that from a homogenous solution. As a result, oiling-out is a common occurrence in LAS processes.

Nevertheless, if the overall composition of the mixture is below the metastable LLE, an amorphous cluster is not self-sustainable, given that its energy level is higher than that of the parent phase. It is unable to continue growing unless it first transforms into a more stable phase. This makes the two-step nucleation closely related to but different from the aforementioned two-step crystallization, where droplets are allowed to continuously grow and rest on the metastable LLE.

7.3.3 Polymorphism

Since SLE is defined by the specific polymorph coexisting with the solution, different polymorphs will intersect the μ_3-x surface (**Figure 4**C) at specific energy levels, with the solubilities following the contours of μ_3-x (**Figure 7**). The chemical potential of a diluted component is dominated by the configuration entropy, plunging down a nearly vertical precipice towards negative infinity. This leads to the solubilities of different polymorphs appearing parallel curves close to linear on the logarithmic scale. A greater energy of dissolution requires more entropy of mixing to compensate, resulting in a lower solubility. The solubility of the stable crystal is the lowest. Conversely, to produce a metastable form, both the concentration and energy levels in the parent phase must exceed the specific SLE.

7.4 Molecular interactions seen from the chemical potential surfaces

A closer examination of **Figure 4** reveals that the vertical precipices of entropy at dilute concentrations are not straight but bending. An inward bend can be seen on the precipice of μ_1-x near the 2-3 edge in **Figure 4**A, reaching up to $x_1 \approx 0.2$. A more pronounced bending of μ_2-x near the 1-3 edge is present in **Figure 4**B, extending further into the Gibbs triangle to $x_2 \approx 0.4$. In both cases, the curvature starts from the edge of infinite dilution and dissipates on the plateau of the μ-x surface at higher concentrations. The boundaries of the bending follow the spinodal curves.

Such deviation from ideal entropy at diluted concentration is the manifestation of the interaction between the other components. At infinite dilution of i, the excess chemical potential of i in mixture i-j-k (Equation (3)) becomes:

$$\begin{aligned}\mu_i^{\mathrm{EX}} = x_j\left(\Omega_{ij} + b_{ij}{x_j}^3\right) + x_k\left(\Omega_{ik} + b_{ik}{x_k}^3\right) - x_j x_k\left(\Omega_{jk} + 4a_{jk}{x_j}^3 + 4b_{jk}{x_k}^3\right) \\ \equiv x_j A_{ij} + x_k A_{ik} - x_j x_k A_{jk}\,,\end{aligned} \tag{10}$$

where $x_j + x_k \approx 1$, and A_{ij} represents the i-j interaction in a general way. Equation (10) shows that μ_i^{EX} at diluted concentration is mainly a linear combination of the i-j and the i-k interactions, subtracted by a non-linear term of j-k interaction. The addition of component i into a mixture of j-k reduces the probability of the j-k interactions but introduces the i-j and the i-k interactions. The curvature of the bending on μ_i at diluted concentration reflects the magnitude of A_{jk}, and its position depends on the asymmetry of A_{jk}.

Equation (10) provides the thermodynamic explanation for the characteristics of parallel solubility curves of the solute polymorphs. Since the interaction energy between cosolvents is weak, **Figure 7** illustrates that μ_3 at low concentrations does exhibit a high degree of linearity on the logarithmic scale, with only a slight upward curvature. Equation (10) shows that the slope of this linearity is given by the difference in the solvent-solute affinities, and the deviation from linearity is the manifestation of the antisolvent-solvent interaction. This relation underlies the log-linear relation of solubility, the parallelism of solubilities of polymorphs, and the insensitivity of the parameters of the J-A model to the nature of the organic solutes. It is this interpretation of the molecular interactions underlying the shape of the solubility curve that allows for the extrapolation of the Gibbs energies and the phase diagram.

Conclusions

To address the competition between oiling-out and crystallization, we have demonstrated that the ternary phase diagram for oiling-out in antisolvent crystallization of a poorly water-soluble solute can be constructed based on a minimum number of experimental measurements. The inputs for the thermodynamic calculations include: the solubility data, the polymorph DSC data, and the cosolvent VLE data. The Jouyban-Acree model and the Gibbs–Helmholtz type equation were used to extract the thermodynamic parameters for the solvent-solute subsystems. With the example system of water-[1,4-dioxane]-DBDCS, we have calculated the spinodal limit, the metastable LLE, and the polymorph SLE at 298.15 K, using a 2-body and 3-body mixing model. Our *in silico* results exhibit satisfactory agreement (**Figure 5**) with the microfluidic phase diagram.

By analyzing the energy associated with composition fluctuations, we suggest the optimal conditions for antisolvent crystallization to be slightly away from the good solvent (**Figure 6**). To promote LLPS, the process design needs to be near the neat antisolvent. The most favorable condition for observing spinodal decomposition is in the intermediate range.

By evaluating the solute chemical potential on the phase diagram (**Figure 7**), we show that a significantly large antisolvent gradient is able of driving and accumulating the solute molecules towards the volume with more good solvent. This antisolvent focusing effect depends on the scale and the magnitude of antisolvent gradient. The energy of disorder upon nucleation is much smaller compared to the solute energy gain upon antisolvent addition. This makes the oiling-out a common occurrence in antisolvent crystallization.

In a metastable solution between the spinodal and the LLPS limits, droplets are favored over crystals; following LLPS, crystals from the droplets are favored over those from the solution. This is a two-step crystallization through LLPS. But from a parent phase below the metastable LLE, an amorphous nucleus is unable to continue growing unless it first transforms into a more stable phase. This makes the two-step nucleation closely related to but different from the aforementioned two-step crystallization.

The solubilities of different polymorphs, including the metastable liquid phase, exhibit parallel close-to-linear curves on the logarithmic scale: the slope of the linearity is given by the difference in the two solvent-solute affinities, and the curvature is the manifestation of the antisolvent-solvent interaction. This thermodynamic explanation underlies the log-linear relation of solubility, the parallelism of the polymorph solubilities, and the insensitivity of the parameters of the J-A model to the nature of the organic solutes.

Based on the above, we suggest that the first factor to be considered in the process design of antisolvent crystallization is the difference in the affinities between the solute and the two solvents, *i.e.,* the solubility ratio, which dominates the thermodynamic behavior of the solute in antisolvent crystallization. The second factor is the antisolvent-solvent ratio, which dominates the competition between oiling-out and crystallization. The third factor is the rates of antisolvent addition and agitation, which manipulates the solute uphill diffusion.

In the framework of CALPHAD, this study provides a comprehensive thermodynamic description of the oiling-out in liquid antisolvent crystallization for water-[1,4-dioxane]-DBDCS. The methodology can be extended to the process design of antisolvent crystallization for other poorly water-soluble organic solutes. However, there are still challenges. Simulation of multicomponent diffusion and crystal growth can be done based on the assessment of the chemical potentials of all components over the Gibbs triangle. The prediction of the polymorph SLE can be tested with *in situ* techniques, such as fluorescence lifetime imaging and X-ray diffraction. For more complex (such as highly soluble, cocrystal, macromolecular, and electrolytic) systems, more sophisticated models and computations may be necessary. In the case of temperature-controlled or supercritical processes, calculations must incorporate temperature or pressure as independent variables. We hope that our contribution can catalyze further thermodynamic and kinetic studies on the competition between oiling-out and crystallization.

Experimental

Materials

DBDCS was synthesized as described in the previous paper[64]. Ultrapure water used in the microfluidic experiment was obtained using a *Milli-Q* filtration system, and 1,4-dioxane from *CARLO ERBA*. The choice of 1,4-dioxane is for its density being close to water.

Microfluidics

The measurement of the microfluidic phase diagram was performed using a coaxial microfluidic mixer. Two capillaries were coaxially aligned: a cylindrical *Polymicro* flexible fused silica capillary (*TSP020090* from *Molex*, inner diameter 20 µm, outer diameter 90 µm) inside a cylindrical borosilicate tube (*CV2033* from *Vitrocom*, inner diameter 200 µm, outer diameter 330 µm). The capillary holder was made from ABS using an *HP Designjet* 3D printer. The solution of DBDCS in 1,4-dioxane was injected through the small capillary in the center into a peripheral flow of a cosolvent mixture. The fraction of water in the peripheral flow was systematically varied from 0 to 100 vol%. The flow rates of the two flows were independently controlled: the central flow with a *Pico Plus Elite* syringe pump (from *Harvard Apparatus*) and the peripheral flow with a *PHD2000* syringe pump (from *Harvard Apparatus*). The central-peripheral flow ratio was systematically changed. The central flow rate was in the range between 100 nL/min to 1000 nL/min, and the peripheral flow rate in the range between 1 µL/min to 10 µL/min.

Optical Microscopy

The phase transitions were observed using a home-modified two-turret inverted microscope (*TE2000-U* from *Nikon)*. The objective used was a *CFI S Plan Fluor ELWD* (from *Nikon*, WD 8.2–6.9 mm, magnification 20x, NA = 0.45, infinite corrected, correction ring range 0–2.6 mm). A parfocal length extender ring of 5 mm thickness was added to match the appropriate focusing distance at the sample plane. Image acquisition was performed using an

Retiga R1 CCD camera (from *Qimaging*, pixel size 6.45 μm), controlled through a *μManager* open-source software.

Birefringence

The birefringence of the phase transitions in the microfluidic system was examined using crossed polarizers on the optical microscope. The illumination source was a tungsten halogen bulb (*EVA64623HLX* from *Osram*, 12 V, 40/CS, 1/SKU, 100 W). Above and below the sample, a pair of polarizer-analyzer were crossed at 90 degrees to create a dark background. The polarizer was a standard multi-coated glass polarizer (*C-SP 754097* from *Nikon*). The analyzer was cut from a *TECHSPEC* visible linear polarizing laminated film (from *Edmund Optics*). The amorphous precipitates remain dark on the dark background, whereas the crystals appear bright due to the birefringence.

Data availability

All data that support the plots within this paper and other finding of this study are available from the corresponding author upon reasonable request.

Code availability

Custom codes for the calculation within this manuscript are available from the corresponding author upon reasonable request.

Associated content

Supporting Information

S.1. Regular solution type model; S.2. VLE of water-[1,4-dioxane] system; S.3. Solubility of DBDCS in water-[1,4-dioxane]; S.4. Gibbs energy of metastable phase; S.5. Thermodynamic parameters; S.6. Phase equilibria; S.7. Energy of composition fluctuation; S.8. Binary subsystems of water-[1,4-dioxane]-DBDCS. (PDF)

Author information

Corresponding Author

*E-mail: zhengyu.zhang@centralesupelec.fr

Declaration of competing interest

The authors declare no competing financial interest.

Author contributions

Zhengyu Zhang: Conceptualization, Methodology, Software, Formal analysis, Investigation, Resources, Data Curation, Writing – Original Draft, Writing – Review & Editing, Visualization. **Ran Bi**: Investigation. **Jean-Frédéric Audibert**: Methodology, Investigation, Resources. **Weixi Wang**: Investigation, Validation, Writing – Review & Editing. **Soo Young Park**: Resources. **Anne Spasojevic-de Biré**: Methodology, Investigation, Writing – Review & Editing, Supervision, Project administration, Funding acquisition. **Robert Bernard Pansu**:

Conceptualization, Methodology, Validation, Investigation, Resources, Writing – Review & Editing, Supervision, Funding acquisition.

Acknowledgement

This work received support from le Laboratoire d’Excellence (LabEx) CHARMMMAT [grant number ANR-11-IDEX-0003-02], l’école doctorale INTERFACES (ED 573), and l’Agence Nationale de la Recherche (ANR) [SUCRINE project, grant number ANR-22-CE51-0023]. Z. Z. would like to thank Melissa Ann Thomas of Université Paris-Saclay’s Academic Writing Center.

Abbreviations

2B3B	2-Body and 3-Body interactional mixing model
ASC	Anti-Solvent Crystallization
ASP	Anti-Solvent Precipitation
CALPHAD	CALculation of PHAse Diagrams
CNIBS/R-K	Combined Nearly Ideal Binary Solvent/Redlich-Kister expression
DBDCS	(2Z,2'Z)-2,2'-(1,4-phenylene)bis(3-(4-butoxyphenyl) acrylonitrile)
DSC	Differential Scanning Calorimetry
G-x	Gibbs energy, G, as a function of composition in amount fraction, x
J-A	Jouyban-Acree Equation
LAS	Liquid Anti-Solvent
LLE	Liquid-Liquid Equilibrium
LLPS	Liquid-Liquid Phase Separation
SLE	Solid-Liquid Equilibrium
VLE	Vapor-Liquid Equilibrium
μ-x	Chemical potential, μ, as a function of amount fraction, x

Nomenclatures

Notation	**Definition**	**Unit**
a_{ij}	Adjustable parameter related to the fraction of component i in i-j interaction in the 2B3B model	$\mathrm{J\cdot mol^{-1}}$
A_{ij}	Binary i-j interaction	$\mathrm{J\cdot mol^{-1}}$
A_n	nth-order adjustable parameter in the J-A equation	K
b_{ij}	Adjustable parameter related to the fraction of component j in i-j interaction in the 2B3B model	$\mathrm{J\cdot mol^{-1}}$
B_n	nth-order adjustable parameter in the CNIBS/R-K expression	$\mathrm{J\cdot mol^{-1}}$
G	Gibbs energy	J
H	Enthalpy	J
p	Pressure	Pa
P_n	nth-order adjustable parameter in Acree's correlation of solubility to the 2B3B parameters	$\mathrm{J\cdot mol^{-1}}$
R	Ideal gas constant, ~8.314 $\mathrm{J\cdot mol^{-1}\cdot K^{-1}}$	$\mathrm{J\cdot mol^{-1}\cdot K^{-1}}$
s	Solubility	Various units
s_i	Solubility in solvent i	Various units
T	Temperature	K
x	Amount fraction	1
μ	Chemical potential	$\mathrm{J\cdot mol^{-1}}$
ρ	Mass concentration	$\mathrm{kg\cdot m^{-3}}$
ϕ	Volume fraction	1
Ω_{ij}	Symmetric adjustable parameter in the 2B3B model	$\mathrm{J\cdot mol^{-1}}$

Super- and sub-scripts	
0	Property at infinite dilute solute concentration
EX	Excess function, deviation from ideal mixture
i	Property of component i
ij	Property of mixture i-j
ijk	Property of mixture i-j-k
is	Property of component i at solubility
isj	Property of component i at solubility in solvent j
$i(\alpha)$	Property of component i in phase α
L	Property of liquid phase
m	Molar property
mix	Property associated with a mixing process
r	Property at room temperature
S	Property of solid phase
$\alpha\leftrightarrow\beta$	Property at equilibrium between phase α and phase β

α→β	Property associated with phase transition α → β
α	Property of phase α

Mathematical notations	
$\mathbf{H}(\quad)$	Hessian matrix of
$\mathbf{x}$	Vector of variables
δ	Small change
Δ	Change, reaction
$(\partial/\partial)_p$	Partial differentiation while holding variable p
$\|\quad\|$	Determinant of a square matrix
$^{\mathrm{T}}$	Transpose of a matrix
$\cdot$	Dot product

References

(1) Göke, K.; Lorenz, T.; Repanas, A.; Schneider, F.; Steiner, D.; Baumann, K.; Bunjes, H.; Dietzel, A.; Finke, J. H.; Glasmacher, B.; et al. Novel strategies for the formulation and processing of poorly water-soluble drugs. *European Journal of Pharmaceutics and Biopharmaceutics* **2018**, *126*, 40-56. DOI: 10.1016/j.ejpb.2017.05.008.

(2) Mellah, D.; Nicolaï, B.; Fournier, B.; Bošnjaković-Pavlović, N.; Legrand, F.-X.; Gemeiner, P.; Boemare, V.; Guiblin, N.; Assi, A.; Tfayli, A.; et al. New Cocrystallization Method: Non-photochemical Laser-Induced Nucleation of a Cocrystal of Caffeine–Gallic Acid in Water. *Crystal Growth & Design* **2022**, *22* (10), 5982-5995. DOI: 10.1021/acs.cgd.2c00624.

(3) Gao, Z.; Rohani, S.; Gong, J.; Wang, J. Recent Developments in the Crystallization Process: Toward the Pharmaceutical Industry. *Engineering* **2017**, *3* (3), 343-353. DOI: 10.1016/j.Eng.2017.03.022.

(4) Rabinow, B. E. Nanosuspensions in drug delivery. *Nat Rev Drug Discov* **2004**, *3* (9), 785-796. DOI: 10.1038/nrd1494.

(5) Mosharraf, M.; Nyström, C. The effect of particle size and shape on the surface specific dissolution rate of microsized practically insoluble drugs. *International Journal of Pharmaceutics* **1995**, *122* (1), 35-47. DOI: 10.1016/0378-5173(95)00033-F.

(6) Censi, R.; Di Martino, P. Polymorph Impact on the Bioavailability and Stability of Poorly Soluble Drugs. *Molecules* **2015**, *20* (10), 18759-18776. DOI: 10.3390/molecules201018759.

(7) Morissette, S. L.; Soukasene, S.; Levinson, D.; Cima, M. J.; Almarsson, O. Elucidation of crystal form diversity of the HIV protease inhibitor ritonavir by high-throughput crystallization. *Proc Natl Acad Sci U S A* **2003**, *100* (5), 2180-2184. DOI: 10.1073/pnas.0437744100.

(8) Veesler, S.; Lafferrère, L.; Garcia, E.; Hoff, C. Phase Transitions in Supersaturated Drug Solution. *Organic Process Research & Development* **2003**, *7* (6), 983-989. DOI: 10.1021/op034089f.

(9) Roelands, C. P. M.; Jiang, S.; Kitamura, M.; ter Horst, J. H.; Kramer, H. J. M.; Jansens, P. J. Antisolvent Crystallization of the Polymorphs ofl-Histidine as a Function of Supersaturation Ratio and of Solvent Composition. *Crystal Growth & Design* **2006**, *6* (4), 955-963. DOI: 10.1021/cg050529d.

(10) Punmalee, N.; Wantha, L.; Flood, A. E. Antisolvent Crystallization of Polymorphs of L-Histidine. *Chemical Engineering & Technology* **2018**, *41* (6), 1132-1138. DOI: 10.1002/ceat.201700676.

(11) Lince, F.; Marchisio, D. L.; Barresi, A. A. Strategies to control the particle size distribution of poly-epsilon-caprolactone nanoparticles for pharmaceutical applications. *J Colloid Interface Sci* **2008**, *322* (2), 505-515. DOI: 10.1016/j.jcis.2008.03.033.

(12) Thorat, A. A.; Dalvi, S. V. Liquid antisolvent precipitation and stabilization of nanoparticles of poorly water soluble drugs in aqueous suspensions: Recent developments and future perspective. *Chemical Engineering Journal* **2012**, *181-182*, 1-34. DOI: 10.1016/j.cej.2011.12.044.

(13) Li, X. S.; Wang, J. X.; Shen, Z. G.; Zhang, P. Y.; Chen, J. F.; Yun, J. Preparation of uniform prednisolone microcrystals by a controlled microprecipitation method. *Int J Pharm* **2007**, *342* (1-2), 26-32. DOI: 10.1016/j.ijpharm.2007.04.025.

(14) Tran, V. L.; Génot, V.; Audibert, J.-F.; Prokazov, Y.; Turbin, E.; Zuschratter, W.; Kim, H.-J.; Jung, J.; Park, S. Y.; Pansu, R. B. Nucleation and growth during a fluorogenic precipitation in a micro-flow mapped by fluorescence lifetime microscopy. *New Journal of Chemistry* **2016**, *40* (5), 4601-4605. DOI: 10.1039/c5nj03400k.

(15) Bhamidi, V.; Lee, S. H.; He, G.; Chow, P. S.; Tan, R. B. H.; Zukoski, C. F.; Kenis, P. J. A. Antisolvent Crystallization and Polymorph Screening of Glycine in Microfluidic Channels Using Hydrodynamic Focusing. *Crystal Growth & Design* **2015**, *15* (7), 3299-3306. DOI: 10.1021/acs.cgd.5b00420.

(16) Génot, V.; Desportes, S.; Croushore, C.; Lefèvre, J.-P.; Pansu, R. B.; Delaire, J. A.; von Rohr, P. R. Synthesis of organic nanoparticles in a 3D flow focusing microreactor. *Chemical Engineering Journal* **2010**, *161* (1-2), 234-239. DOI: 10.1016/j.cej.2010.04.029.

(17) Tao, J.; Chow, S. F.; Zheng, Y. Application of flash nanoprecipitation to fabricate poorly water-soluble drug nanoparticles. *Acta Pharm Sin B* **2019**, *9* (1), 4-18. DOI: 10.1016/j.apsb.2018.11.001.

(18) Durelle, M.; Charton, S.; Gobeaux, F.; Chevallard, C.; Belloni, L.; Testard, F.; Trépout, S.; Carriere, D. Coexistence of Transient Liquid Droplets and Amorphous Solid Particles in Nonclassical Crystallization of Cerium Oxalate. *The Journal of Physical Chemistry Letters* **2022**, *13* (36), 8502-8508. DOI: 10.1021/acs.jpclett.2c01829.

(19) Sun, M.; Du, S.; Chen, M.; Rohani, S.; Zhang, H.; Liu, Y.; Sun, P.; Wang, Y.; Shi, P.; Xu, S.; et al. Oiling-Out Investigation and Morphology Control of β-Alanine Based on Ternary Phase Diagrams. *Crystal Growth & Design* **2018**, *18* (2), 818-826. DOI: 10.1021/acs.cgd.7b01293.

(20) Veesler, S.; Revalor, E.; Bottini, O.; Hoff, C. Crystallization in the Presence of a Liquid−Liquid Phase Separation. *Organic Process Research & Development* **2006**, *10* (4), 841-845. DOI: 10.1021/op060085+.

(21) Deneau, E.; Steele, G. An In-Line Study of Oiling Out and Crystallization. *Organic Process Research & Development* **2005**, *9* (6), 943-950. DOI: 10.1021/op050107c.

(22) Sun, M.; Tang, W.; Du, S.; Zhang, Y.; Fu, X.; Gong, J. Understanding the Roles of Oiling-out on Crystallization of β-Alanine: Unusual Behavior in Metastable Zone Width and Surface Nucleation during Growth Stage. *Crystal Growth & Design* **2018**, *18* (11), 6885-6890. DOI: 10.1021/acs.cgd.8b01096.

(23) Myerson, A. S.; Trout, B. L. Chemistry. Nucleation from solution. *Science* **2013**, *341* (6148), 855-856. DOI: 10.1126/science.1243022.

(24) Galkin, O.; Vekilov, P. G. Are Nucleation Kinetics of Protein Crystals Similar to Those of Liquid Droplets? *Journal of the American Chemical Society* **2000**, *122* (1), 156-163. DOI: 10.1021/ja9930869.

(25) Zhang, F. Nonclassical nucleation pathways in protein crystallization. *J Phys Condens Matter* **2017**, *29* (44), 443002. DOI: 10.1088/1361-648X/aa8253.

(26) Vekilov, P. G. Nucleation. *Crystal Growth & Design* **2010**, *10* (12), 5007-5019. DOI: 10.1021/cg1011633.

(27) Lafferrère, L.; Hoff, C.; Veesler, S. In Situ Monitoring of the Impact of Liquid−Liquid Phase Separation on Drug Crystallization by Seeding. *Crystal Growth & Design* **2004**, *4* (6), 1175-1180. DOI: 10.1021/cg0497750.

(28) Zhao, H.; Xie, C.; Xu, Z.; Wang, Y.; Bian, L.; Chen, Z.; Hao, H. Solution Crystallization of Vanillin in the Presence of a Liquid–Liquid Phase Separation.

Industrial & Engineering Chemistry Research **2012**, *51* (45), 14646-14652. DOI: 10.1021/ie302360u.

(29) Tanaka, K.; Takiyama, H. Effect of Oiling-Out during Crystallization on Purification of an Intermediate Compound. *Organic Process Research & Development* **2019**, *23* (9), 2001-2008. DOI: 10.1021/acs.oprd.9b00256.

(30) Parimaladevi, P.; Supriya, S.; Srinivasan, K. The role of ultrasound in controlling the liquid-liquid phase separation and nucleation of vanillin polymorphs I and II. *Journal of Crystal Growth* **2018**, *484*, 21-30. DOI: 10.1016/j.jcrysgro.2017.12.023.

(31) Gao, Z.; Altimimi, F.; Gong, J.; Bao, Y.; Wang, J.; Rohani, S. Ultrasonic Irradiation and Seeding To Prevent Metastable Liquid–Liquid Phase Separation and Intensify Crystallization. *Crystal Growth & Design* **2018**, *18* (4), 2628-2635. DOI: 10.1021/acs.cgd.8b00284.

(32) Frontana-Uribe, B. A.; Moreno, A. On Electrochemically Assisted Protein Crystallization and Related Methods†. *Crystal Growth & Design* **2008**, *8* (12), 4194-4199. DOI: 10.1021/cg800731p.

(33) Hammadi, Z.; Astier, J.-P.; Morin, R.; Veesler, S. p. Spatial and Temporal Control of Nucleation by Localized DC Electric Field. *Crystal Growth & Design* **2009**, *9* (8), 3346-3347. DOI: 10.1021/cg900150n.

(34) Gowayed, O. Y.; Moosa, T.; Moratos, A. M.; Hua, T.; Arnold, S.; Garetz, B. A. Dynamic Light Scattering Study of a Laser-Induced Phase-Separated Droplet of Aqueous Glycine. *The Journal of Physical Chemistry B* **2021**, *125* (28), 7828-7839. DOI: 10.1021/acs.jpcb.1c02620.

(35) Walton, F.; Wynne, K. Control over phase separation and nucleation using a laser-tweezing potential. *Nat Chem* **2018**, *10* (5), 506-510. DOI: 10.1038/s41557-018-0009-8.

(36) Lafferrère, L.; Hoff, C.; Veesler, S. Study of liquid–liquid demixing from drug solution. *Journal of Crystal Growth* **2004**, *269* (2-4), 550-557. DOI: 10.1016/j.jcrysgro.2004.05.048.

(37) Yang, H.; Rasmuson, Å. C. Investigation of Batch Cooling Crystallization in a Liquid–Liquid Separating System by PAT. *Organic Process Research & Development* **2012**, *16* (6), 1212-1224. DOI: 10.1021/op200355b.

(38) Lai, S. M.; Yuen, M. Y.; Siu, L. K. S.; Ng, K. M.; Wibowo, C. Experimental determination of solid-liquid-liquid equilibrium phase diagrams. *AIChE Journal* **2007**, *53* (6), 1608-1619. DOI: 10.1002/aic.11183.

(39) Li, X.; Yin, Q.; Zhang, M.; Hou, B.; Bao, Y.; Gong, J.; Hao, H.; Wang, Y.; Wang, J.; Wang, Z. Process Design for Antisolvent Crystallization of Erythromycin Ethylsuccinate in Oiling-out System. *Industrial & Engineering Chemistry Research* **2016**, *55* (27), 7484-7492. DOI: 10.1021/acs.iecr.6b00795.

(40) Yang, H.; Rasmuson, Å. C. Phase equilibrium and mechanisms of crystallization in liquid–liquid phase separating system. *Fluid Phase Equilibria* **2015**, *385*, 120-128. DOI: 10.1016/j.fluid.2014.11.007.

(41) Yang, H.; Rasmuson, Å. C. Ternary phase diagrams of ethyl paraben and propyl paraben in ethanol aqueous solvents. *Fluid Phase Equilibria* **2014**, *376*, 69-75. DOI: 10.1016/j.fluid.2014.05.036.

(42) Kiesow, K.; Tumakaka, F.; Sadowski, G. Experimental investigation and prediction of oiling out during crystallization process. *Journal of Crystal Growth* **2008**, *310* (18), 4163-4168. DOI: 10.1016/j.jcrysgro.2008.06.034.

(43) Espitalier, F.; Biscans, B.; Peyrigain, P. S.; Laguérie, C. Ternary diagram: alpha-(3-benzoylphenyl)-propionic acid (ketoprofen) in acetone water

mixtures at different temperatures. Experimental data and predicted results. *Fluid Phase Equilibria* **1995**, *113* (1-2), 151-171. DOI: 10.1016/0378-3812(95)02806-8.

(44) Taratuta, V. G.; Holschbach, A.; Thurston, G. M.; Blankschtein, D.; Benedek, G. B. Liquid-liquid phase separation of aqueous lysozyme solutions: effects of pH and salt identity. *The Journal of Physical Chemistry* **1990**, *94* (5), 2140-2144. DOI: 10.1021/j100368a074.

(45) Kiesow, K.; Ruether, F.; Sadowski, G. Solubility, crystallization and oiling-out behavior of PEGDME: 1. Pure-solvent systems. *Fluid Phase Equilibria* **2010**, *298* (2), 253-261. DOI: 10.1016/j.fluid.2010.08.005.

(46) Ilevbare, G. A.; Taylor, L. S. Liquid–Liquid Phase Separation in Highly Supersaturated Aqueous Solutions of Poorly Water-Soluble Drugs: Implications for Solubility Enhancing Formulations. *Crystal Growth & Design* **2013**, *13* (4), 1497-1509. DOI: 10.1021/cg301679h.

(47) de Albuquerque, I.; Mazzotti, M. Crystallization Process Design Using Thermodynamics To Avoid Oiling Out in a Mixture of Vanillin and Water. *Crystal Growth & Design* **2014**, *14* (11), 5617-5625. DOI: 10.1021/cg500904v.

(48) Varela de Albuquerque, I. Design of Crystallization Processes in Mixtures that Exhibit Liquid-Liquid Phase Separation. ETH Zurich, 2018 DOI: 10.3929/ethz-b-000323112.

(49) Bhamidi; Abolins. A Thermodynamic Approach for the Prediction of Oiling Out Boundaries from Solubility Data. *Processes* **2019**, *7* (9), 577. DOI: 10.3390/pr7090577.

(50) Gibbs, J. W. On the equilibrium of heterogeneous substances. *Transactions of the Connecticut Academy of Arts and Sciences* **1876**, *3*, 108–248.

(51) Meijering, J. Segregation in regular ternary solutions. *Philips research reports* **1950**, *5*, 333-356.

(52) Meijering, J. SEGREGATION IN REGULAR TERNARY SOLUTIONS. 2. *Philips research reports* **1951**, *6* (3), 183-210.

(53) Cahn, J. W. On spinodal decomposition. *Acta Metallurgica* **1961**, *9* (9), 795-801. DOI: 10.1016/0001-6160(61)90182-1.

(54) Cahn, J. W.; Hilliard, J. E. Free Energy of a Nonuniform System. I. Interfacial Free Energy. *The Journal of Chemical Physics* **1958**, *28* (2), 258-267. DOI: 10.1063/1.1744102.

(55) Cahn, J. W.; Hilliard, J. E. Free Energy of a Nonuniform System. III. Nucleation in a Two ‐ Component Incompressible Fluid. *The Journal of Chemical Physics* **1959**, *31* (3), 688-699. DOI: 10.1063/1.1730447 (acccessed 2022/03/04).

(56) Kattner, U. R.; Campbell, C. E. Invited review: Modelling of thermodynamics and diffusion in multicomponent systems. *Materials Science and Technology* **2013**, *25* (4), 443-459. DOI: 10.1179/174328408x372001.

(57) Jouyban, A.; Shayanfar, A.; Panahi-Azar, V.; Soleymani, J.; Yousefi, B. H.; Acree, W. E., Jr.; York, P. Solubility prediction of drugs in mixed solvents using partial solubility parameters. *J Pharm Sci* **2011**, *100* (10), 4368-4382. DOI: 10.1002/jps.22589.

(58) Dadmand, S.; Kamari, F.; Acree, W. E., Jr.; Jouyban, A. Solubility Prediction of Drugs in Binary Solvent Mixtures at Various Temperatures Using a Minimum Number of Experimental Data Points. *AAPS PharmSciTech* **2018**, *20* (1), 10. DOI: 10.1208/s12249-018-1244-4.

(59) Jouyban, A.; Acree, W. E. Mathematical derivation of the Jouyban-Acree model to represent solute solubility data in mixed solvents at various temperatures.

Journal of Molecular Liquids **2018**, *256*, 541-547. DOI: 10.1016/j.molliq.2018.01.171.

(60) Acree, W. E. Mathematical representation of thermodynamic properties. *Thermochimica Acta* **1992**, *198* (1), 71-79. DOI: 10.1016/0040-6031(92)85059-5.

(61) Hwang, C.-A.; Holste, J. C.; Hall, K. R.; Ali Mansoori, G. A simple relation to predict or to correlate the excess functions of multicomponent mixtures. *Fluid Phase Equilibria* **1991**, *62* (3), 173-189. DOI: 10.1016/0378-3812(91)80009-k.

(62) Zhang, Z. Laser-Induced Nucleation in a Coaxial Microfluidic Mixer. Université Paris Saclay (COmUE), Gif-sur-Yvette, Essonne, 2019, http://www.theses.fr/2019SACLN023.

(63) Álvarez-Asencio, R.; Moreno-Ramírez, J. S.; Pimentel, C.; Casado, S.; Matta, M.; Gierschner, J.; Muccioli, L.; Yoon, S.-J.; Varghese, S.; Park, S. Y.; et al. Molecular-scale shear response of the organic semiconductor β-DBDCS (100) surface. *Physical Review B* **2017**, *96* (11), 115422. DOI: 10.1103/PhysRevB.96.115422.

(64) Yoon, S. J.; Chung, J. W.; Gierschner, J.; Kim, K. S.; Choi, M. G.; Kim, D.; Park, S. Y. Multistimuli two-color luminescence switching via different slip-stacking of highly fluorescent molecular sheets. *J Am Chem Soc* **2010**, *132* (39), 13675-13683. DOI: 10.1021/ja1044665.

(65) Yalkowsky, S. H.; Rubino, J. T. Solubilization by cosolvents I: organic solutes in propylene glycol-water mixtures. *J Pharm Sci* **1985**, *74* (4), 416-421. DOI: 10.1002/jps.2600740410.

(66) Jouyban, A.; Acree, W. E., Jr. In silico prediction of drug solubility in water-ethanol mixtures using Jouyban-Acree model. *J Pharm Pharm Sci* **2006**, *9* (2), 262-269. https://www.ncbi.nlm.nih.gov/pubmed/16959195.

(67) Jouyban, A. Solubility prediction of drugs in water-polyethylene glycol 400 mixtures using Jouyban-acree model. *Chem Pharm Bull (Tokyo)* **2006**, *54* (11), 1561-1566. DOI: 10.1248/cpb.54.1561.

(68) Jouyban, A. Prediction of drug solubility in water-propylene glycol mixtures using Jouyban-Acree model. *Die Pharmazie - An International Journal of Pharmaceutical Sciences* **2007**, *62* (5), 365-367. DOI: 10.1691/ph.2007.5.6176.

(69) Jouyban, A. In silico prediction of drug solubility in water-dioxane mixtures using the Jouyban-Acree model. *Die Pharmazie - An International Journal of Pharmaceutical Sciences* **2007**, *62* (1), 46-50. DOI: 10.1691/ph2007.1.6057.

(70) Jouyban-Gharamaleki, A.; Barzegar-Jalali, M.; Acree, W. E. Solubility correlation of structurally related drugs in binary solvent mixtures. *International Journal of Pharmaceutics* **1998**, *166* (2), 205-209. DOI: 10.1016/S0378-5173(98)00044-1.

(71) Jouyban-Gharamaleki, A.; Acree, W. E. Comparison of models for describing multiple peaks in solubility profiles. *International Journal of Pharmaceutics* **1998**, *167* (1), 177-182. DOI: 10.1016/S0378-5173(98)00073-8.

(72) Jouyban-Gharamaleki, A. Comparison of various cosolvency models for calculating solute solubility in water–cosolvent mixtures. *International Journal of Pharmaceutics* **1999**, *177* (1), 93-101. DOI: 10.1016/s0378-5173(98)00333-0.

(73) Jouyban-Gharamaleki, A.; York, P.; Hanna, M.; Clark, B. J. Solubility prediction of salmeterol xinafoate in water--dioxane mixtures. *Int J Pharm* **2001**, *216* (1-2), 33-41. DOI: 10.1016/s0378-5173(00)00694-3.

(74) Jouyban-Gharamaleki, A. A novel method for improvement of predictability of the CNIBS/R-K equation. *International Journal of Pharmaceutics* **1997**, *154* (2), 245-247. DOI: 10.1016/s0378-5173(97)00136-1.

(75) Jouyban, A. Review of the cosolvency models for predicting solubility of drugs in water-cosolvent mixtures. *J Pharm Pharm Sci* **2008**, *11* (1), 32-58. DOI: 10.18433/j3pp4k (acccessed 2020/01/14).

(76) Jouyban, A.; Shokri, J.; Barzegar-Jalali, M.; Hassanzadeh, D.; Acree, W. E.; Ghafourian, T.; Nokhodchi, A. Solubility of Chlordiazepoxide, Diazepam, and Lorazepam in Ethanol + Water Mixtures at 303.2 K. *Journal of Chemical & Engineering Data* **2009**, *54* (7), 2142-2145. DOI: 10.1021/je900200k.

(77) Jouyban, A.; Acree, W. E. Prediction of drug solubility in ethanol-ethyl acetate mixtures at various temperatures using the Jouyban-Acree model. *Journal of Drug Delivery Science and Technology* **2007**, *17* (2), 159-160. DOI: 10.1016/s1773-2247(07)50025-0.

(78) Zhou, Z.; Qu, Y.; Wang, J.; Wang, S.; Liu, J.; Wu, M. Measurement and Correlation of Solubilities of (Z)-2-(2-Aminothiazol-4-yl)-2-methoxyiminoacetic Acid in Different Pure Solvents and Binary Mixtures of Water + (Ethanol, Methanol, or Glycol). *Journal of Chemical & Engineering Data* **2011**, *56* (4), 1622-1628. DOI: 10.1021/je101351w.

(79) Jouyban, A.; Khoubnasabjafari, M.; Chan, H. K.; Acree, W. E., Jr. Mathematical representation of solubility of amino acids in binary aqueous-organic solvent mixtures at various temperatures using the Jouyban-Acree model. *Pharmazie* **2006**, *61* (9), 789-792. https://pubmed.ncbi.nlm.nih.gov/17020157/ From NLM.

(80) Bowden, N. A.; Sevillano, D. M.; Sanders, J. P. M.; Bruins, M. E. Modelling the effects of ethanol on the solubility of the proteinogenic amino acids with the NRTL, Gude and Jouyban-Acree models. *Fluid Phase Equilibria* **2018**, *459*, 158-169. DOI: 10.1016/j.fluid.2017.11.036.

(81) Khoubnasabjafari, M.; Jouyban, A.; Acree, W. E., Jr. Mathematical representation of solubility of electrolytes in binary solvent mixtures using Jouyban-Acree model. *Chem Pharm Bull (Tokyo)* **2005**, *53* (12), 1591-1593. DOI: 10.1248/cpb.53.1591.

(82) Vierk, A.-L. Experimentelle Untersuchungen an den Zweistoffsystemen: Wasser-Acetonitril, Wasser-Dioxan, Äthanol-Acetonitril und Cyclohexan-Dioxan. *Zeitschrift für anorganische Chemie* **1950**, *261* (5-6), 283-296. DOI: 10.1002/zaac.19502610504.

(83) Goates, J. R.; Sullivan, R. J. Thermodynamic Properties of the System Water-p-Dioxane. *The Journal of Physical Chemistry* **1958**, *62* (2), 188-190. DOI: 10.1021/j150560a011.

(84) Turnbull, D. Formation of Crystal Nuclei in Liquid Metals. *Journal of Applied Physics* **1950**, *21* (10), 1022-1028. DOI: 10.1063/1.1699435.

(85) Hoffman, J. D. Thermodynamic Driving Force in Nucleation and Growth Processes. *The Journal of Chemical Physics* **1958**, *29* (5), 1192-1193. DOI: 10.1063/1.1744688 (acccessed 2020/01/28).

(86) Suzuki, T.; Fujisawa, M.; Takagi, S.; Kimura, T. Excess enthalpies of water+1,4-dioxane at 278.15, 298.15, 318.15 and 338.15 K. *Journal of Thermal Analysis and Calorimetry* **2006**, *85* (3), 545-550, journal article. DOI: 10.1007/s10973-006-7658-3.

(87) Krishna, R. Serpentine diffusion trajectories and the Ouzo effect in partially miscible ternary liquid mixtures. *Phys Chem Chem Phys* **2015**, *17* (41), 27428-27436. DOI: 10.1039/c5cp04520g.

For table of contents use only

Thermodynamics of oiling-out in antisolvent crystallization. I. Extrapolation of ternary phase diagram from solubility to instability

Zhengyu Zhang[1,2,3*], Ran Bi[4], Jean-Frédéric Audibert[3,4], Weixi Wang[5], Soo Young Park[6], Anne Spasojevic-de Biré[1], Robert Bernard Pansu[2,3]

[1] Université Paris-Saclay, CentraleSupélec, CNRS, Laboratoire SPMS, 91190 Gif-sur-Yvette, France
[2] Université Paris-Saclay, CNRS, Ecole Normale Supérieure Paris-Saclay, CentraleSupélec, Laboratoire LuMIn, 91190 Gif-sur-Yvette, France
[3] Université Paris Saclay, Institut d'Alembert (IDA), CNRS, Ecole Normale Supérieure Paris-Saclay, 91190 Gif-sur-Yvette, France
[4] Université Paris-Saclay, CNRS, Ecole Normale Supérieure Paris-Saclay, Laboratoire PPSM, 91190 Gif-sur-Yvette, France
[5] École polytechnique, LPICM, CNRS, Institut Polytechnique de Paris, 91120 Palaiseau, France
[6] Department of Materials Science and Engineering, Seoul National University, 1 Gwanak-ro, Gwanak-gu, Seoul 151-744, Korea

*Correspond to: zhengyu.zhang@centralesupelec.fr

TOC graphic

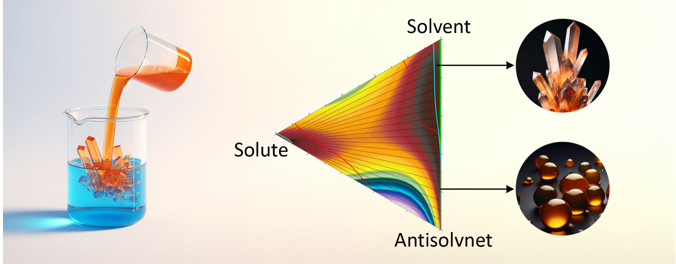

Synopsis

The competition between oiling-out and crystallization poses a significant challenge in the antiviolent crystallization of poorly soluble solutes. Thermodynamic calculation of the phase diagram offers guidance for the process design. The predictions agree with the phase diagram measured through microfluidics.

For journal front art

Antisolvent crystallization vs oiling-out, a dance of two rivals. How to tackle this challenge? Thermodynamics and microfluidics can cross-validate and guide the process design.

Supporting Information

Thermodynamics of oiling-out in antisolvent crystallization. I. Extrapolation of ternary phase diagram from solubility to instability

Zhengyu Zhang[1,2,3*], Ran Bi[4], Jean-Frédéric Audibert[3,4], Weixi Wang[5], Soo Young Park[6], Anne Spasojevic-de Biré[1], Robert Bernard Pansu[2,3]

[1] Université Paris-Saclay, CentraleSupélec, CNRS, Laboratoire SPMS, 91190 Gif-sur-Yvette, France
[2] Université Paris-Saclay, CNRS, Ecole Normale Supérieure Paris-Saclay, CentraleSupélec, Laboratoire LuMIn, 91190 Gif-sur-Yvette, France
[3] Université Paris Saclay, Institut d'Alembert (IDA), CNRS, Ecole Normale Supérieure Paris-Saclay, 91190 Gif-sur-Yvette, France
[4] Université Paris-Saclay, CNRS, Ecole Normale Supérieure Paris-Saclay, Laboratoire PPSM, 91190 Gif-sur-Yvette, France
[5] École polytechnique, LPICM, CNRS, Institut Polytechnique de Paris, 91120 Palaiseau, France
[6] Department of Materials Science and Engineering, Seoul National University, 1 Gwanak-ro, Gwanak-gu, Seoul 151-744, Korea

*Correspond to: zhengyu.zhang@centralesupelec.fr

Table of content

S.1 Regular solution type model

The regular solution type model are commonly used in CALPHAD for liquid mixtures.[1] In binary systems, these models regard the excess Gibbs energy as the enthalpy of mixing, for example, in the form of a Redlich-Kister type polynomial:

$$G_{ij,\mathrm{m}}^{\mathrm{EX}} = H_{ij,\mathrm{m}}^{\mathrm{EX}} = x_i x_j \sum_{n=0}^{N} \Omega_n \left(x_j - x_i\right)^n , \tag{S1}$$

where $G_{ij,\mathrm{m}}^{\mathrm{EX}}$ denotes the excess molar Gibbs energy of the *i-j* mixture, $H_{ij,\mathrm{m}}^{\mathrm{EX}}$ the molar enthalpy of mixing, x_i represents the amount fraction of component *i*, N is the order of the polynomial, and Ω_n the adjustable parameters.

The 2B3B model is essentially a third-order regular solution type model, as its enthalpic term can be rearranged into a Redlich-Kister type polynomial:

$$x_i x_j \left(\Omega_{ij} + a_{ij} {x_i}^3 + b_{ij} {x_j}^3\right) = x_i x_j \sum_{n=0}^{3} \Omega_n \left(x_j - x_i\right)^n , \tag{S2}$$

where Ω_{ij}, a_{ij} and b_{ij} are the adjustable parameters of the 2B3B model (*cf.* Section 2.1), and

$$\begin{aligned} -8\Omega_3 &= a_{ij} - b_{ij} \ , \\ 4\Omega_2 + 12\Omega_3 &= 3b_{ij} \ , \\ -2\Omega_1 - 4\Omega_2 - 6\Omega_3 &= -3b_{ij} \ , \\ \Omega_0 + \Omega_1 + \Omega_2 + \Omega_3 &= b_{ij} + \Omega_{ij} \ . \end{aligned}$$

The 2B3B model may not be superior than other higher-order regular solution type models, but the derived J-A model allows for the optimization of thermodynamic parameters from the low solubility.

The simplest regular solution model has only the symmetric zeroth-order parameter in the enthalpic term. The parameter Ω_0 is interpreted to be the binary "interaction energy". The higher the positive interaction energy, the stronger the repulsion between the two components, and *vice versa* the attraction. **Figure S1** illustrates that the *G*-*x* (molar Gibbs energy, *G*, as a function of amount fraction composition, *x*) curve for a hypothetical binary solution with $\Omega_0 <$

$2RT$ is convex, the system being stable for the whole composition range. A miscibility gap starts to appear when $\Omega_0 > 2RT$. An interaction energy of $\Omega_0 > 5RT$ is large enough to result in minuscule mutual miscibility.

The Gibbs energy of the binary subsystems of water (1)-[1,4-dioxane] (2)-DBDCS (3) are plotted in **Figure S1**, labeled as "1-2", "2-3", and "1-3", to compare with the regular solutions. The height of water (1) -DBDCS (3) system is close to that of a regular solution with $\Omega_0 = 9.5RT$ but exhibits apparent asymmetry. The system of [1,4-dioxane] (2)-DBDCS (3) is quite symmetric and close to a regular solution with $\Omega_0 = 4.5RT$. The system of water (1)-[1,4-dioxane] (2) is convex but close to separation as it is just below the threshold of thermodynamic instability: $\Omega_0 = 2RT$.

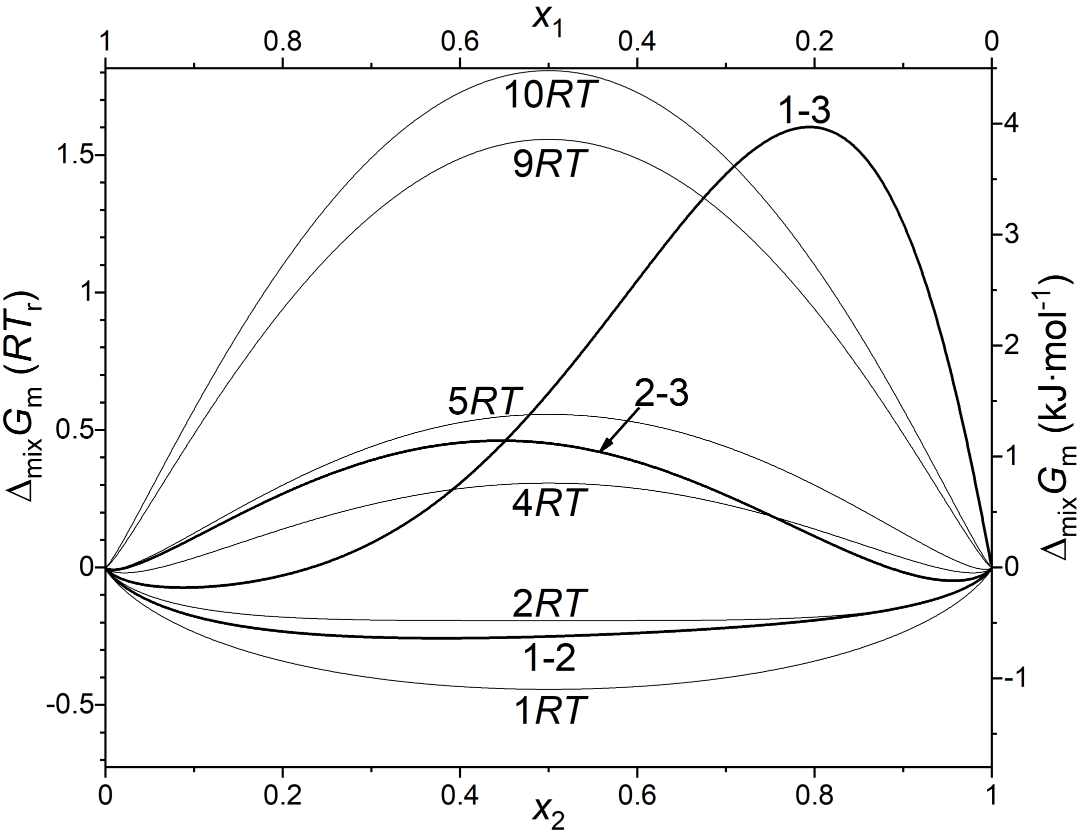

Figure S1. Molar Gibbs energy of mixing, $\Delta_{\text{mix}}G_{\text{m}}$, of some theoretical zeroth-order regular binary solutions at 298.15 K, plotted against the amount-fraction composition x, with the interaction energy Ω_0 labeled in RT next to the curves. The $\Delta_{\text{mix}}G_{\text{m}}$ for the binary subsystems of water (1)-[1,4-dioxane] (2)-DBDCS (3) at 298.15 K are plotted for comparison, labeled as “1-2”, “2-3”, and “1-3”. $RT_{\text{r}} \approx 2.5\text{kJ}\cdot\text{mol}^{-1}$.

S.2 VLE of water-[1,4-dioxane] system

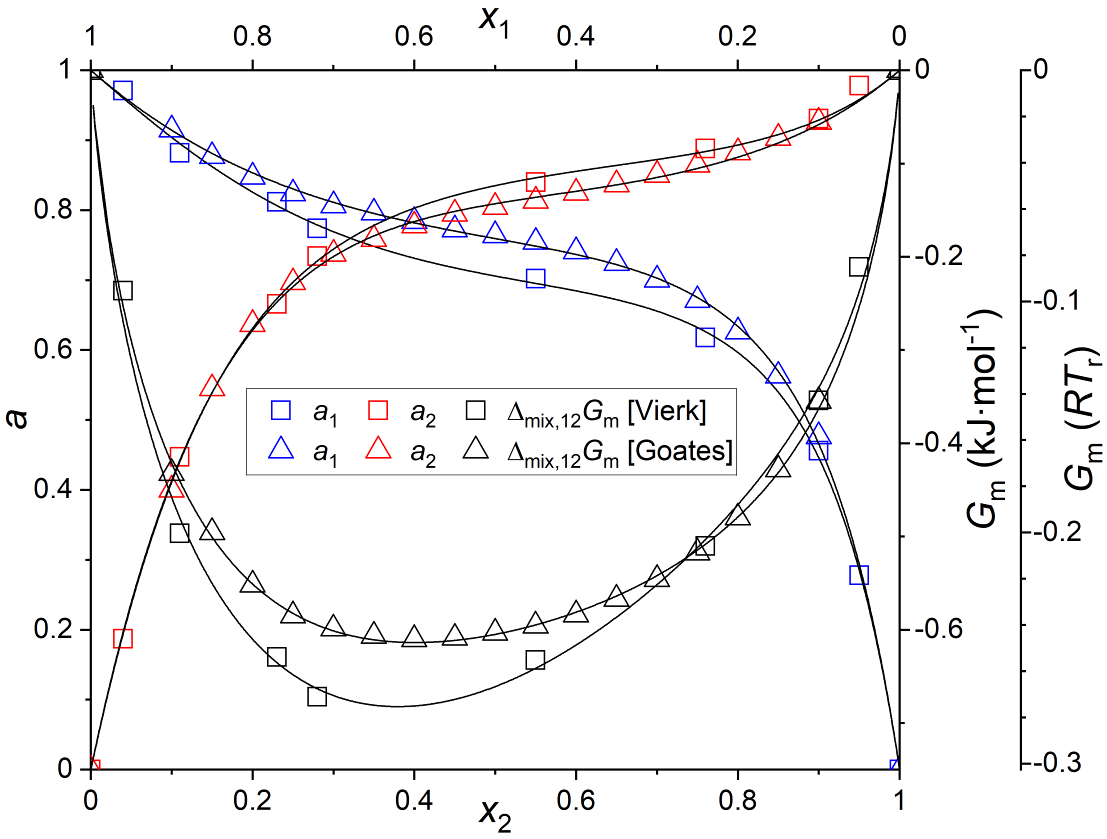

Figure S2. VLE of water (1)-[1,4-dioxane] (2) binary system in term of amount-fraction composition x at 298.15 K, data measured by Vierk[2] (square) and Goates[3] (triangle), fitted to the 2B3B model. The partial pressures are presented as activities, a. The total pressures are plotted as the molar Gibbs energy of mixing, $\Delta_{\mathrm{mix}}G_{12,\mathrm{m}}$. $RT_{\mathrm{r}} \approx 2.5\mathrm{kJ} \cdot \mathrm{mol}^{-1}$.

S.3 Solubility of DBDCS in water-[1,4-dioxane]

The solubility of the γ phase of DBDCS (3) in water (1)-[1,4-dioxane] (2) mixture was measured at 298.15 K[†] as a function of solvent composition. Ultrapure water obtained through a *Milli-Q* filtration system was used as the antisolvent, and 1,4-dioxane from *CARLO ERBA* as the "good" solvent. DBDCS (3) is fluorescent in crystal but not in solution. The good solvent was incrementally added and fully agitated into a saturated solution in contact with undissolved DBDCS (3) until the complete dissolution was indicated by the fluorescence. The fluorescence was excited using the 4W 365nm tube of a *VL-4.LC* UV lamp (from *VILBER LOURMAT*). The quantities of the three components were measured by weighing on an *Xroyal 205 SM-DR* analytic balance (from *Precisa*). The mass fraction solubility, $w_{3\mathrm{s}}$, was recorded. Subsequently, the antisolvent was added in small amounts into the mixture and fully agitated until the precipitate was detected by the fluorescence. The processes of dissolution and precipitation were repeated in the range of $w_{3\mathrm{s}} > 2\mathrm{x}10^{-5}$ and $\phi_2^0 > 0.7$, below which $w_{3\mathrm{s}}$ was too small to be weighed. After that, the amount-concentration solubility, c_{3s}, was determined by absorption spectroscopy using a *Cary 4000 UV-Vis* spectrophotometer (from *Agilent*), with the molar extinction coefficient of DBDCS (3) measured to be $26287 \pm 119\ \mathrm{L/(mol \cdot cm)}$ at $354\ \mathrm{nm}$. Finally, the solubility in neat water (1), $x_{3\mathrm{s}1}$, was even below the detection limit of the spectrophotometer. It was extrapolated using the J-A Equation (5) with Jouyban's[4] adjustable parameters for water (1)-[1,4-diosane] (2) systems: $A_0 = 2206.9\ \mathrm{K}$, $A_1 = 1173.1\ \mathrm{K}$, $A_2 = 1997.4\ \mathrm{K}$. The solubility data were converted to the amount-fraction solubility, $x_{3\mathrm{s}}$, as plotted in **Figure S3** and listed in **Table S1**.

[†] The digits in the temperature do not indicate the precision.

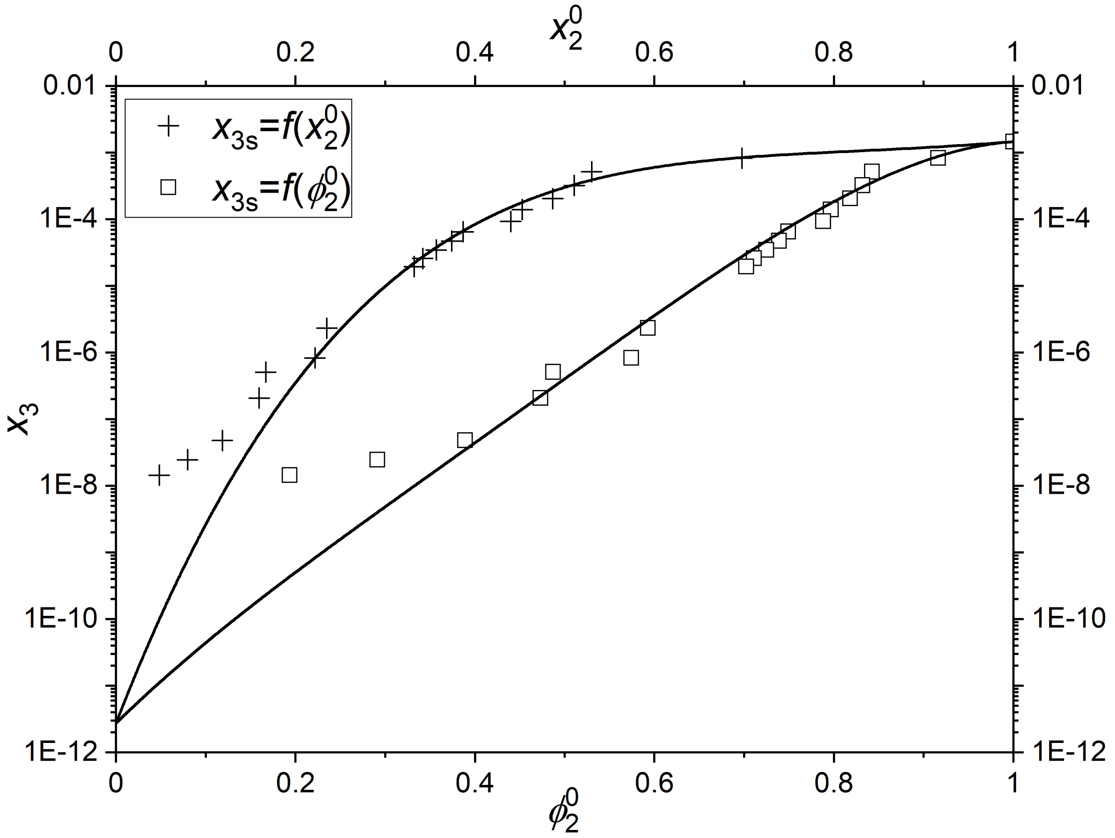

Figure S3. Amount-fraction solubility x_{3s} of DBDCS (3) in the mixture of water (1)-[1,4-dioxane] (2) at 298.15 K. The same data are plotted twice against the top and bottom abscissa: the top abscissa is the solute-free amount fraction of 1,4-dioxane (2), x_2^0, for fitting with the CNIBS/R-K Equation (6); the bottom abscissa is the solute-free volume fraction, ϕ_2^0, for fitting with the Acree-Jouyban Equation (5).

Table S1.[‡] Solubility data of DBDCS (3) in water (1)-[1,4-dioxane] (2) at 298.15 K, as a function of the solute-free volume fraction of 1,4-dioxane (2), ϕ_2^0.

ϕ_2^0	1	0.916259216	0.842431275	0.831882398	0.818106607
w_{3s}	0.00789063	0.00587209	0.00442982	0.00285311	0.00187558
x_{3s}	0.001456632	0.000823851	0.000512514	0.000322055	0.000205158
ϕ_2^0	0.796884019	0.788288668	0.749431892	0.739125625	0.724717933
w_{3s}	0.00132982	0.00090138	0.00068778	0.00050741	0.00038425
x_{3s}	0.000138818	9.23852E-05	6.51279E-05	4.70966E-05	3.47032E-05
ϕ_2^0	0.711153883	0.702421288			
w_{3s}	0.00029373	0.00022338			
x_{3s}	2.58705E-05	1.93651E-05			
ϕ_2^0	0.574463713	0.473290719	0.592943323	0.487316982	0.389159419
$c_{3s}/[\mathrm{mol/l}]$	2.55545E-05	7.34774E-06	0.00007	1.76894E-05	1.86404E-06
x_{3s}	8.27961E-07	2.07785E-07	2.33051E-06	5.09162E-07	4.77325E-08
ϕ_2^0	0.29146736	0.19387463	0		
$c_{3s}/[\mathrm{mol/l}]$	1.06517E-06	6.84749E-07			
x_{3s}	2.46179E-08	1.44464E-08	2.73179E-12 ±9.37968E-13		

[‡] The solubility was measured in mass fraction solubility, w_{3s}, in the range of $\phi_2^0 > 0.7$, by weighing, and in amount-concentration solubility, c_{3s}, in the range of $\phi_2^0 < 0.7$, by absorption spectroscopy. The solubility in neat water (1) was below the detection limit and was extrapolated using the Jouyban-Acree equation. The solubility data were converted to the amount-fraction solubility, x_{3s}.

S.4 Gibbs energy of metastable phase

If phase α of a pure substance transforms into phase β upon heating, at the equilibrium temperature $T_{\alpha\leftrightarrow\beta}$, the molar Gibbs energy of the phase transition $\Delta_{\alpha\rightarrow\beta}G_\mathrm{m}\left(T_{\alpha\leftrightarrow\beta}\right)$ is zero. The enthalpy of transition, $\Delta_{\alpha\rightarrow\beta}H_\mathrm{m}\left(T_{\alpha\leftrightarrow\beta}\right)$, can be measured. The molar entropy of transition at $T_{\alpha\leftrightarrow\beta}$ is:

$$\Delta_{\alpha\rightarrow\beta}S_\mathrm{m}(T_{\mathrm{S}\leftrightarrow\mathrm{L}}) = \frac{\Delta_{\alpha\rightarrow\beta}H_\mathrm{m}\left(T_{\alpha\leftrightarrow\beta}\right)}{T_{\alpha\leftrightarrow\beta}}. \tag{S3}$$

If the heat capacities of the two phases are known from $T_{\alpha\leftrightarrow\beta}$ to T, accurate $\Delta_{\alpha\rightarrow\beta}H_\mathrm{m}(T)$ and $\Delta_{\alpha\rightarrow\beta}S_\mathrm{m}(T)$ can be calculated:

$$\begin{aligned}\Delta_{\alpha\rightarrow\beta}H_\mathrm{m}(T) &= \Delta_{\alpha\rightarrow\beta}H_\mathrm{m}\left(T_{\alpha\leftrightarrow\beta}\right) + \int_{T_{\alpha\leftrightarrow\beta}}^{T} \Delta_{\alpha\rightarrow\beta}c_\mathrm{m}(T)dT \ , \\ \Delta_{\alpha\rightarrow\beta}S_\mathrm{m}(T) &= \Delta_{\alpha\rightarrow\beta}S_\mathrm{m}\left(T_{\alpha\leftrightarrow\beta}\right) + \int_{T_{\alpha\leftrightarrow\beta}}^{T} \Delta_{\alpha\rightarrow\beta}c_\mathrm{m}(T)d\ln T \ ,\end{aligned} \tag{S4}$$

where $\Delta_{\alpha\rightarrow\beta}c_\mathrm{m}(T) \equiv c_{\beta,\mathrm{m}}(T) - c_{\alpha,\mathrm{m}}(T)$ is the difference in the molar heat capacities of the two phases. The energy of the metastable phase relative to the stable one is therefore:

$$\Delta_{\alpha\rightarrow\beta}G_\mathrm{m}(T) \ = \Delta_{\alpha\rightarrow\beta}H_\mathrm{m}(T) - T\Delta_{\alpha\rightarrow\beta}S_\mathrm{m}(T) \ . \tag{S5}$$

In the absence of such data, $\Delta_{\alpha\rightarrow\beta}G_\mathrm{m}(T)$ can be assessed resorting to the integral form of the Gibbs-Helmholtz Equation (8). In the study on the driving force of homogeneous nucleation in supercooled metal droplets, Turnbull[5] got:

$$\begin{aligned}\Delta_{\mathrm{S}\rightarrow\mathrm{L}}G_\mathrm{m}(T) &\approx \Delta_{\mathrm{S}\rightarrow\mathrm{L}}H_\mathrm{m}(T_{\mathrm{S}\leftrightarrow\mathrm{L}})\frac{\Delta T}{T_{\mathrm{S}\leftrightarrow\mathrm{L}}} \\ &= \Delta_{\mathrm{S}\rightarrow\mathrm{L}}S_\mathrm{m}(T_{\mathrm{S}\leftrightarrow\mathrm{L}})\Delta T \ ,\end{aligned} \tag{S6}$$

where $\Delta_{\mathrm{S}\rightarrow\mathrm{L}}G_\mathrm{m}(T)$ is the molar Gibbs energy of fusion, S stands for solid, L for liquid, $T_{\mathrm{S}\leftrightarrow\mathrm{L}}$ denotes the melting temperature, and $\Delta T \equiv T_{\mathrm{S}\leftrightarrow\mathrm{L}} - T$ is the supercooling. This is the definite integral of the Gibbs-Helmholtz equation, from $T_{\mathrm{S}\leftrightarrow\mathrm{L}}$ to T, assuming temperature independent $\Delta_{\mathrm{S}\rightarrow\mathrm{L}}S_\mathrm{m}$ and $\Delta_{\mathrm{S}\rightarrow\mathrm{L}}H_\mathrm{m}$, *i.e.* $\Delta_{\mathrm{S}\rightarrow\mathrm{L}}c_\mathrm{m} \approx 0$. This simplest formula has been widely used.

Nevertheless, under large supercooling, the temperature dependence of $\Delta_{\mathrm{S}\to\mathrm{L}}S_{\mathrm{m}}$ and $\Delta_{\mathrm{S}\to\mathrm{L}}H_{\mathrm{m}}$ is more pronounced[6]. Assuming an linear temperature dependence of $\Delta_{\mathrm{S}\to\mathrm{L}}H_{\mathrm{m}}(T)$, *i.e.* temperature independent nonzero $\Delta_{\mathrm{S}\to\mathrm{L}}c_{\mathrm{m}}$, Hoffman[7] obtained:

$$\begin{aligned}\Delta_{\mathrm{S}\to\mathrm{L}}G_{\mathrm{m}}(T) &= \frac{\Delta_{\mathrm{S}\to\mathrm{L}}H_{\mathrm{m}}(T_{\mathrm{S}\leftrightarrow\mathrm{L}})T\Delta T}{{T_{\mathrm{S}\leftrightarrow\mathrm{L}}}^2} \\ &= \frac{\Delta_{\mathrm{S}\to\mathrm{L}}S_{\mathrm{m}}(T_{\mathrm{S}\leftrightarrow\mathrm{L}})T\Delta T}{T_{\mathrm{S}\leftrightarrow\mathrm{L}}}\ . \end{aligned} \tag{S7}$$

Hoffman's equation is more accurate between $T_{\mathrm{S}\leftrightarrow\mathrm{L}}$ and the glass transition temperature of the metastable liquid for materials with large $\Delta_{\mathrm{S}\to\mathrm{L}}c_{\mathrm{m}}$, such as water[8] and o-terphenyl[9, 10].

The Gibbs energy of DBDCS in different states as functions of temperature are schematically illustrated in **Figure S4**. From the DSC data[11] of the polymorphs of DBDCS, we used Turnbull's formula (S6) to assess $\Delta_{\gamma\to\beta}G_{\mathrm{m}}(T) \approx 1.1RT_{\mathrm{r}}$, between the two polymorphs, and Hoffman's equation (S7) to assess $\Delta_{\beta\to\mathrm{L}}G_{\mathrm{m}}(T) \approx 2.5RT_{\mathrm{r}}$, between the β phase and the metastable liquid. Their sum gives $\Delta_{\gamma\to\mathrm{L}}G_{\mathrm{m}}(T) \approx 3.6RT_{\mathrm{r}}$, between the γ phase and the metastable liquid.

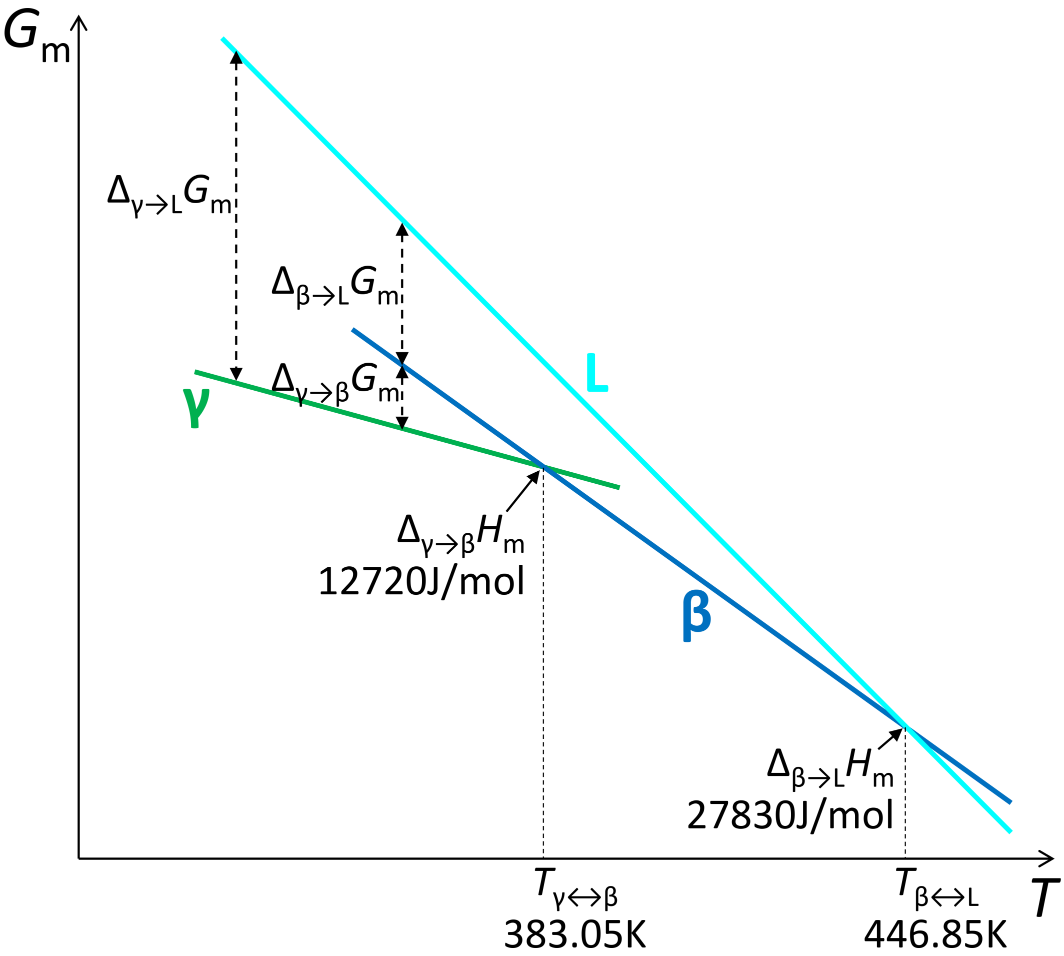

Figure S4. Schematic illustration of the molar Gibbs energy, G_m, of DBDCS in different states as functions of temperature, T. The γ phase of DBDCS is at equilibrium with the β phase at 383.05 K. The β phase is at equilibrium with the liquid phase, L, at 446.85 K. The DSC data[11] of the latent heat are marked at the corresponding positions.

S.5 Thermodynamic parameters

Table S2.[§] Thermodynamic parameters for the phase diagram calculation of water (1)-[1,4-dioxane] (2)-DBDCS (3) ternary system at 298.15 K.

Parameter		Ω_{12}	a_{12}	b_{12}
Model		2B3B eq. (3)		
Data		VLE[2]: a_1		
Fit	/[J·mol^{-1}]	4153±61	-1031±196	877±134
	/[RT_r]	1.675	-0.416	0.354
Model		2B3B eq. (3)		
Data		VLE[2]: a_2		
Fit	/[J·mol^{-1}]	4447±48	-256±143	1148±195
	/[RT_r]	1.794	-0.103	0.463
Model		2B3B eq. (1)		
Data		VLE[2]: $\Delta_{\text{mix}}G_{12,\text{m}}$		
Fit	/[J·mol^{-1}]	4080±130	-297±313	1492±324
	/[RT_r]	1.646	-0.120	0.602
Model		2B3B eq. (3)		
Data		VLE[3]: a_1		
Fit	/[J·mol^{-1}]	4388±17	-160±64	659±64
	/[RT_r]	1.770	-0.065	0.266
Model		2B3B eq. (3)		
Data		VLE[3]: a_2		
Fit	/[J·mol^{-1}]	4443±20	-209±77	557±72
	/[RT_r]	1.792	-0.084	0.225
Model		2B3B eq. (1)		
Data		VLE[3]: $\Delta_{\text{mix}}G_{12,\text{m}}$		
Fit	/[J·mol^{-1}]	4378±13	-146±38	744±38
	/[RT_r]	1.766	-0.059	0.300
Use	/[J·mol^{-1}]	4314.730992	-349.9321233	912.7824617
	/[RT_r]	1.740542874	-0.141161028	0.368212297

Parameter		a_{13}	a_{23}
Model		J-A eq. (6)	
Data		SLE: $x_{3\text{s}}$	
Fit	/[J·mol^{-1}]	50098±1108	-4752±874
	/[RT_r]	20.209	-1.917
Use	/[J·mol^{-1}]	50098.20063	-4752.16073
	/[RT_r]	20.20938646	-1.917000042
Parameter		Ω_{13}	Ω_{23}
Model		J-A eq. (9)	
Data		SLE: $x_{3\text{s}1}$	SLE: $x_{3\text{s}2}$
Use	/[J·mol^{-1}]	9726.658501	14763.77726
	/[RT_r]	3.923689836	5.955640652
Parameter		b_{13}	b_{23}
Model		Regular solution eq. (S1)	
Data			
Use	/[J·mol^{-1}]	0	0
	/[RT_r]	0	0
Parameter		$\Delta_{\beta\rightarrow\text{L}}G_{3,\text{m}}(T_r)$	
Model		Hoffman's eq. (S7)	
Data		DSC[11]	
Use	/[J·mol^{-1}]	6180.009501	
	/[RT_r]	2.492987747	
Parameter		$\Delta_{\gamma\rightarrow\text{L}}G_{3,\text{m}}(T_r)$	
Model		Turnbull's eq. (S6) Hoffman's eq. (S7)	
Data		DSC[11]	
Use	/[J·mol^{-1}]	8999.397426	
	/[RT_r]	3.630316023	

[§] The values used in the calculations are labeled as "Use". The number of digits is not an indication of the precision but for the consistency of the numerical computation. The parameters are extracted from the data of three sets of independent experiments, as separated in the table: Ω_{12}, a_{12}, and b_{12} from the VLE data of water (1)-[1,4-dioxane] (2); a_{23}, a_{13}, Ω_{13}, and Ω_{23} from the solubility data; $\Delta_{\gamma\rightarrow\text{L}}G_{3,\text{m}}(T)$ and $\Delta_{\beta\rightarrow\text{L}}G_{3,\text{m}}(T)$ from the DSC data. The 1-2 parameters were determined as the average of the fittings of six sets of VLE data from two independent measurements: activity a_1 as the partial pressure of water (1), a_2 as the partial pressure of 1,4-dioxane (2), and $\Delta_{\text{mix}}G_{12,\text{m}}$ taking into account of both partial pressures. The uncertainties of the adjustable parameters were provided by the fitting software, using the dispersion of the experimental points relative to the model as an estimation of the measurement error.

S.6 Phase equilibria

Gibbs[12] established that the necessary and sufficient conditions for a system of n components to be at thermodynamic equilibrium in φ homogeneous phases, "uninfluenced by gravity, electricity, distortion of the solid masses, or capillary tensions":

$$\begin{gathered} T_\alpha = T_\beta = \cdots = T_\varphi \ , \\ p_\alpha = p_\beta = \cdots = p_\varphi \ , \\ \begin{cases} \mu_{1(\alpha)} = \mu_{1(\beta)} = \cdots = \mu_{1(\varphi)} \ , \\ \mu_{2(\alpha)} = \mu_{2(\beta)} = \cdots = \mu_{2(\varphi)} \ , \\ \qquad \vdots \\ \mu_{n(\alpha)} = \mu_{n(\beta)} = \cdots = \mu_{n(\varphi)} \ , \end{cases} \end{gathered} \tag{S8}$$

where T_α and p_α denote the temperature and pressure of phase α, and $\mu_{i(\alpha)}$ is the chemical potential of component i in phase α.

For the equilibrium between two ternary phases, every root of Equation (S8) defines a pair of mutually saturated solutions. The *G-x* (Gibbs energy, G, as a function of composition in amount fraction, x) surface of the system is touched by a double tangent plane at the compositions of each pair of the coexisting phases. The parent phase prior to the separation sits on the tie-line that connects the double tangent pair, with the equilibrium phase proportions governed by the lever rule. The collection of the conjugated tangent pairs on one isothermal section constitutes the binodal curves at the given p and T. The ensemble of the binodal curves over T forms the binodal surfaces on a polythermal ternary phase diagram.

S.7 Energy of composition fluctuation

Gibbs[12] demonstrated that the necessary and sufficient conditions of the internal thermodynamic stability of a homogeneous multicomponent system be that the chemical potential of each component increases with its amount of substance[13]. The local curvature of a function $f(\mathbf{x})$ is described by its Hessian matrix, $\boldsymbol{\nabla}^{\mathrm{T}} \cdot \boldsymbol{\nabla} f(\mathbf{x})$. It is strictly convex if $\boldsymbol{\nabla}^{\mathrm{T}} \cdot \boldsymbol{\nabla} f(\mathbf{x})$ is positive definite, strictly concave if $\boldsymbol{\nabla}^{\mathrm{T}} \cdot \boldsymbol{\nabla} f(\mathbf{x})$ is negative definite, and concave-convex (saddle) if $\boldsymbol{\nabla}^{\mathrm{T}} \cdot \boldsymbol{\nabla} f(\mathbf{x})$ is indefinite. The Hessian matrix of the molar Gibbs energy in terms of composition is:

$$\mathbf{H}(G_{\mathrm{m}}) \equiv \boldsymbol{\nabla}^{\mathrm{T}} \cdot \boldsymbol{\nabla} G_{\mathrm{m}}(\mathbf{x}) = \begin{bmatrix} \dfrac{{\partial_{!n}}^{2} G_{\mathrm{m}}}{\partial {x_1}^{2}} & \dfrac{{\partial_{!n}}^{2} G_{\mathrm{m}}}{\partial x_1 \partial x_2} & \cdots & \dfrac{{\partial_{!n}}^{2} G_{\mathrm{m}}}{\partial x_1 \partial x_{n-1}} \\ \dfrac{{\partial_{!n}}^{2} G_{\mathrm{m}}}{\partial x_2 \partial x_1} & \dfrac{{\partial_{!n}}^{2} G_{\mathrm{m}}}{\partial {x_2}^{2}} & \cdots & \dfrac{{\partial_{!n}}^{2} G_{\mathrm{m}}}{\partial x_2 \partial x_{n-1}} \\ \vdots & \vdots & \ddots & \vdots \\ \dfrac{{\partial_{!n}}^{2} G_{\mathrm{m}}}{\partial x_{n-1} \partial x_1} & \dfrac{{\partial_{!n}}^{2} G_{\mathrm{m}}}{\partial x_{n-1} \partial x_2} & \cdots & \dfrac{{\partial_{!n}}^{2} G_{\mathrm{m}}}{\partial {x_{n-1}}^{2}} \end{bmatrix}, \qquad \text{(S9)}$$

where x_i denotes the amount fraction of component i, n is the number of components, and the partial derivative $\partial_{!n}/\partial x_i \equiv (\partial/\partial x_i)_{p,T,x_j,j\neq i,n}$ with any $n-1$ of the n components being independent variables and an arbitrary component n being constrained by $\sum_i x_i = 1$. The limit of the instability of a homogeneous mixture (with composition fluctuations) is the Hessian determinant of the molar Gibbs energy being zero[12].

$$|\mathbf{H}(G_{\mathrm{m}})| = 0\,. \qquad (S10)$$

The Gibbs energy change associated with an infinitesimal composition fluctuation can be evaluated through the curvature of the *G*-*x* surface. In a homogeneous multicomponent mixture of composition $\mathbf{x}$, the energy of an infinitesimal composition fluctuation $\delta\mathbf{x}$ is expressed by the Taylor expansion of the Gibbs energy, $G_{\mathrm{m}}(\mathbf{x})$:

$$G_{\mathrm{m}}(\mathbf{x} + \delta\mathbf{x}) = G_{\mathrm{m}}(\mathbf{x}) + \boldsymbol{\nabla} G_{\mathrm{m}}(\mathbf{x})^{\mathrm{T}} \delta\mathbf{x} + \frac{1}{2} \delta\mathbf{x}^{\mathrm{T}} \mathbf{H}\big(G_{\mathrm{m}}(\mathbf{x})\big) \delta\mathbf{x} + \cdots\ , \qquad (S11)$$

where $\boldsymbol{\nabla} G_{\mathrm{m}}(\mathbf{x})$ is the gradient of the molar Gibbs energy of the mixture in terms of composition $\mathbf{x}$. Say $\delta\mathbf{x}$ is compensated by its vicinities that sum up to $-\delta\mathbf{x}$ due to mass conservation, the energy of the compensating vicinities is:

$$G_{\mathrm{m}}(\mathbf{x}-\delta\mathbf{x}) = G_{\mathrm{m}}(\mathbf{x}) - \boldsymbol{\nabla} G_{\mathrm{m}}(\mathbf{x})^{\mathrm{T}}\delta\mathbf{x} + \frac{1}{2}\delta\mathbf{x}^{\mathrm{T}}\mathbf{H}\big(G_{\mathrm{m}}(\mathbf{x})\big)\delta\mathbf{x} + \cdots \ . \tag{S12}$$

Therefore, the total energy change of system caused by such a fluctuation is:

$$\delta G_{\mathrm{m}} = \delta\mathbf{x}^{\mathrm{T}}\mathbf{H}\big(G_{\mathrm{m}}(\mathbf{x})\big)\delta\mathbf{x} \ . \tag{S13}$$

Along the concave directions the *G-x*, an infinitesimal composition fluctuation leads to reduced G_{m}, resulting in spontaneous amplification and spread of spinodal decomposition. Therefore, the homogeneous mixture is anywhere instable in the concave and the concave-convex domains of the *G-x* surface. In the convex domain, infinitesimal composition fluctuations along every direction increases G_{m} , the system being resistant to small perturbations in the absence of a second phase. In the convex domain, even though more stable states may exist, the mixture itself may stay metastable for a significant duration due to the kinetic hindrance in the redistribution of matter. For a phase transition to initiate below the instability limit, Gibbs had considered a fluctuation large in degree but small in extent, which led to the classical nucleation theory.

The direction of a fluctuation can be random. The "volume" of a linear transformation is its determinant, the product of the eigenvalues, each of which acts as a scaling factor that stretches or squishes an eigen dimension. In the case where $\mathbf{H}\big(G_{\mathrm{m}}(\mathbf{x})\big)$ is positive definite and the direction of the composition fluctuation is random, we can use the Hessian determinant $|\mathbf{H}(G_{\mathrm{m}})|$ as an indicator for the average energy gain associated with the fluctuation and thus for the resistance of the homogeneous system to perturbations.

S.8 Binary subsystems of water-[1,4-dioxane]-DBDCS

The three binary edges of the ternary phase diagram of water (1)-[1,4-dioxane] (2)-DBDCS (3) at 298.15 K are presented in **Figure S5**. The full miscibility of the binary system water (1)-[1,4-dioxane] (2) is demonstrated by the convex $\Delta_{\mathrm{mix}}G_{12,\mathrm{m}}$ and the positive $d^2\Delta_{\mathrm{mix}}G_{12,\mathrm{m}}/dx_i{}^2$ throughout the entire composition range. Both μ_1 and μ_2 monotonically increase with their respective amount fractions. The molecular interaction is asymmetric. The intersection of the two *μ*-*x* curves coincides with the minimum of $\Delta_{\mathrm{mix}}G_{12,\mathrm{m}}$ at $x_2 \approx 0.379$. The system is close to separation within the intermediate composition range of $\sim 0.4 < x_2 < \sim 0.7$, indicated by the positive yet close-to-zero $d^2\Delta_{\mathrm{mix}}G_{12,\mathrm{m}}/dx_i{}^2$ and $d\mu_i/dx_i$. Positive but close-to-zero $d^2\Delta_{\mathrm{mix}}G_{\mathrm{m}}/dx_i{}^2$ means that an infinitesimal fluctuation in composition scarcely increases the energy of the system; and positive but close-to-zero $d\mu_i/dx_i$ indicates that the chemical potential increases slightly with its amount fraction. Under the same concentration gradient, the thermodynamic driving force of diffusion will be much smaller in the range of $\sim 0.4 < x_2 < \sim 0.7$ compared to the regions outside of it but still downhill towards homogeneity.

Figure S5B and C show that the poorly soluble solute-solvent binary systems are more complex than the fully miscible solvents. The *G*-*x* curve changes its convexity simultaneously as the *μ*-*x* curves change their monotonicity, as shown by that the $d^2\Delta_{\mathrm{mix}}G_{\mathrm{m}}/dx_i{}^2$ and the two $d\mu_i/dx_i$ share the same intercepts with zero: $x_1 \approx 0.589$ and $x_3 \approx 0.006$ for water (1)-DBDCS (3) in **Figure S5**B, and $x_2 \approx 0.114$ and $x_3 \approx 0.228$ for [1,4-dioxane] (2)-DBDCS (3) in **Figure S5**C. These are the spinodal limits in the binary systems. Between the spinodal limits is the spinodal decomposition region, shown in cinnamon background, where $d^2\Delta_{\mathrm{mix}}G_{\mathrm{m}}/dx_i{}^2 < 0$ (instability) and $d\mu_i/dx_i < 0$ (uphill diffusion).

The tie-lines of the metastable LLE touch the $\Delta_{\mathrm{mix}}G_{\mathrm{m}}$ at: $x_1 \approx 0.097$ and $x_3 \approx 9.5\mathrm{E}-11$ for water (1)-DBDCS (3) in **Figure S5**B, and $x_2 \approx 0.008$ and $x_3 \approx 0.045$ for [1,4-dioxane] (2)-DBDCS (3) in **Figure S5**C. Between the spinodal decomposition limit and the LLE binodal is the LLPS region, shown in green background color. The intersections of μ_3 with the DBDCS (3) polymorphs ($-2.5RT_\mathrm{r}$ for the γ phase and $-3.6RT_\mathrm{r}$ for the β phase, relative to the liquid state,) give the γ SLE at $x_3 \approx 0.001$ and the β SLE at $x_3 \approx 0.004$ in [1,4-dioxane] (2), and both SLE practically zero in water (1). Between the metastable LLE and the SLE is the crystallization region, indicated by the cyan background. On the solvent-rich right side, the crystallization region is defined between the solubilities of the solute liquid and the solute crystal in the solvent; on the solute-rich left side, it reflects the saturated concentration of the solvent in the metastable liquid solute. The crystallization domain of DBDCS (3) in water (1), on the right of **Figure S5**B, is too minuscule to be seen.

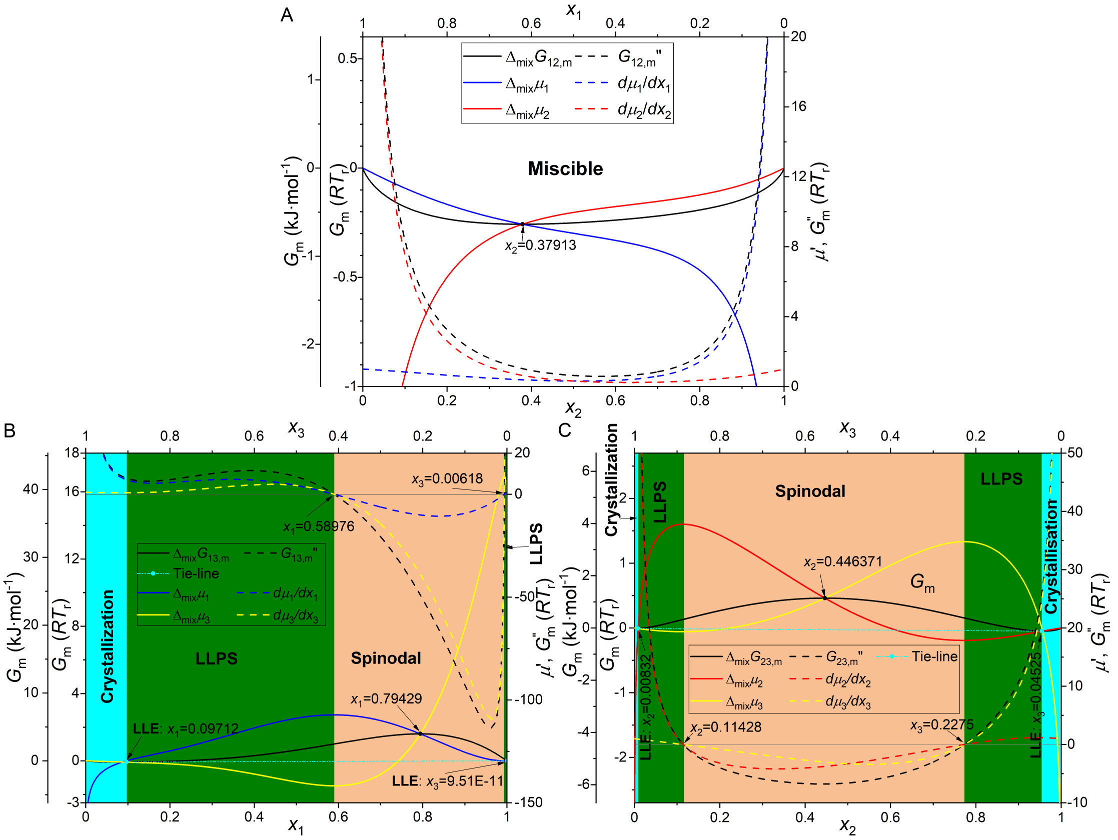

Figure S5. Gibbs energies of mixing, relative to the liquid reference states, of binary subsystems of water (1)-[1,4-dioxane] (2)-DBDCS (3) at 298.15 K, plotted against amount fraction composition x. A: 1-2; B: 1-3; C: 2-3. The black curves represent properties of the mixtures, blue for partial properties of water (1), red for dioxane (2), and yellow for DBDCS (3). The $\Delta_{\text{mix}}G_{ij,\text{m}}$ represents the molar Gibbs energy of mixing of *i*-*j*, $\Delta_{\text{mix}}G_{ij,\text{m}}''$ is the second derivative of the Gibbs energy in terms of composition, and $\Delta_{\text{mix}}\mu_i$ is the chemical potential of component *i*. The compositions of the maxima, the inflection points (spinodal decomposition limits), and the double tangent points (LLE) of $\Delta_{\text{mix}}G_{ij,\text{m}}$ are labeled at the corresponding positions. The background colors indicate: white for miscible region, cyan for crystallization region, green for LLPS region, and cinnamon for spinodal decomposition region. The solubilities and the dissolution regions are too low to be visible. $RT_{\text{r}} \approx 2.5\text{kJ} \cdot \text{mol}^{-1}$.

References

(1) Kattner, U. R.; Campbell, C. E. Invited review: Modelling of thermodynamics and diffusion in multicomponent systems. *Materials Science and Technology* **2013**, *25* (4), 443-459. DOI: 10.1179/174328408x372001.

(2) Vierk, A.-L. Experimentelle Untersuchungen an den Zweistoffsystemen: Wasser-Acetonitril, Wasser-Dioxan, Äthanol-Acetonitril und Cyclohexan-Dioxan. *Zeitschrift für anorganische Chemie* **1950**, *261* (5-6), 283-296. DOI: 10.1002/zaac.19502610504.

(3) Goates, J. R.; Sullivan, R. J. Thermodynamic Properties of the System Water-p-Dioxane. *The Journal of Physical Chemistry* **1958**, *62* (2), 188-190. DOI: 10.1021/j150560a011.

(4) Jouyban, A. In silico prediction of drug solubility in water-dioxane mixtures using the Jouyban-Acree model. *Die Pharmazie - An International Journal of Pharmaceutical Sciences* **2007**, *62* (1), 46-50. DOI: 10.1691/ph2007.1.6057.

(5) Turnbull, D. Formation of Crystal Nuclei in Liquid Metals. *Journal of Applied Physics* **1950**, *21* (10), 1022-1028. DOI: 10.1063/1.1699435.

(6) Kauzmann, W. The Nature of the Glassy State and the Behavior of Liquids at Low Temperatures. *Chemical Reviews* **1948**, *43* (2), 219-256. DOI: 10.1021/cr60135a002.

(7) Hoffman, J. D. Thermodynamic Driving Force in Nucleation and Growth Processes. *The Journal of Chemical Physics* **1958**, *29* (5), 1192-1193. DOI: 10.1063/1.1744688 (acccessed 2020/01/28).

(8) Toner, M.; Cravalho, E. G.; Karel, M. Thermodynamics and kinetics of intracellular ice formation during freezing of biological cells. *Journal of Applied Physics* **1990**, *67* (3), 1582-1593. DOI: 10.1063/1.345670 (acccessed 2020/06/14).

(9) Greet, R. J.; Turnbull, D. Glass Transition in o‐Terphenyl. *The Journal of Chemical Physics* **1967**, *46* (4), 1243-1251. DOI: 10.1063/1.1840842 (acccessed 2020/06/14).

(10) Thompson, C. V.; Spaepen, F. On the approximation of the free energy change on crystallization. *Acta Metallurgica* **1979**, *27* (12), 1855-1859. DOI: 10.1016/0001-6160(79)90076-2.

(11) Yoon, S. J.; Chung, J. W.; Gierschner, J.; Kim, K. S.; Choi, M. G.; Kim, D.; Park, S. Y. Multistimuli two-color luminescence switching via different slip-stacking of highly fluorescent molecular sheets. *J Am Chem Soc* **2010**, *132* (39), 13675-13683. DOI: 10.1021/ja1044665.

(12) Gibbs, J. W. On the equilibrium of heterogeneous substances. *Transactions of the Connecticut Academy of Arts and Sciences* **1876**, *3*, 108–248.

(13) Cahn, J. W. On spinodal decomposition. *Acta Metallurgica* **1961**, *9* (9), 795-801. DOI: 10.1016/0001-6160(61)90182-1.

Supporting Information for Review Only

Thermodynamics of oiling-out in antisolvent crystallization. I. Extrapolation of ternary phase diagram from solubility to instability

Zhengyu Zhang[1,2,3*], Ran Bi[4], Jean-Frédéric Audibert[3,4], Weixi Wang[5], Soo Young Park[6], Anne Spasojevic-de Biré[1], Robert Bernard Pansu[2,3]

[1] Université Paris-Saclay, CentraleSupélec, CNRS, Laboratoire SPMS, 91190 Gif-sur-Yvette, France
[2] Université Paris-Saclay, CNRS, Ecole Normale Supérieure Paris-Saclay, CentraleSupélec, Laboratoire LuMIn, 91190 Gif-sur-Yvette, France
[3] Université Paris Saclay, Institut d'Alembert (IDA), CNRS, Ecole Normale Supérieure Paris-Saclay, 91190 Gif-sur-Yvette, France
[4] Université Paris-Saclay, CNRS, Ecole Normale Supérieure Paris-Saclay, Laboratoire PPSM, 91190 Gif-sur-Yvette, France
[5] École polytechnique, LPICM, CNRS, Institut Polytechnique de Paris, 91120 Palaiseau, France
[6] Department of Materials Science and Engineering, Seoul National University, 1 Gwanak-ro, Gwanak-gu, Seoul 151-744, Korea

*Correspond to: zhengyu.zhang@centralesupelec.fr

The phase diagram of antisolvent crystallization of DBDCS in water-[1,4-dioxane] was measured in a coaxial microfluidic device, as shown in **Figure SR1**. The central jet is DBDCS dissolved in 1,4-dioxane. It is injected into a peripheral flow of a mixture of water and 1,4-dioxane. The transient phase transitions were followed for typically less than 10 seconds along the microfluidic channel after the mixing nozzle. Crystallization and precipitation were observed under different conditions. The phase diagram was explored by systematically changing the flow rates and the fraction of the antisolvent. The crystals and the amorphous precipitates were discerned by their birefringence under crossed polarizers.

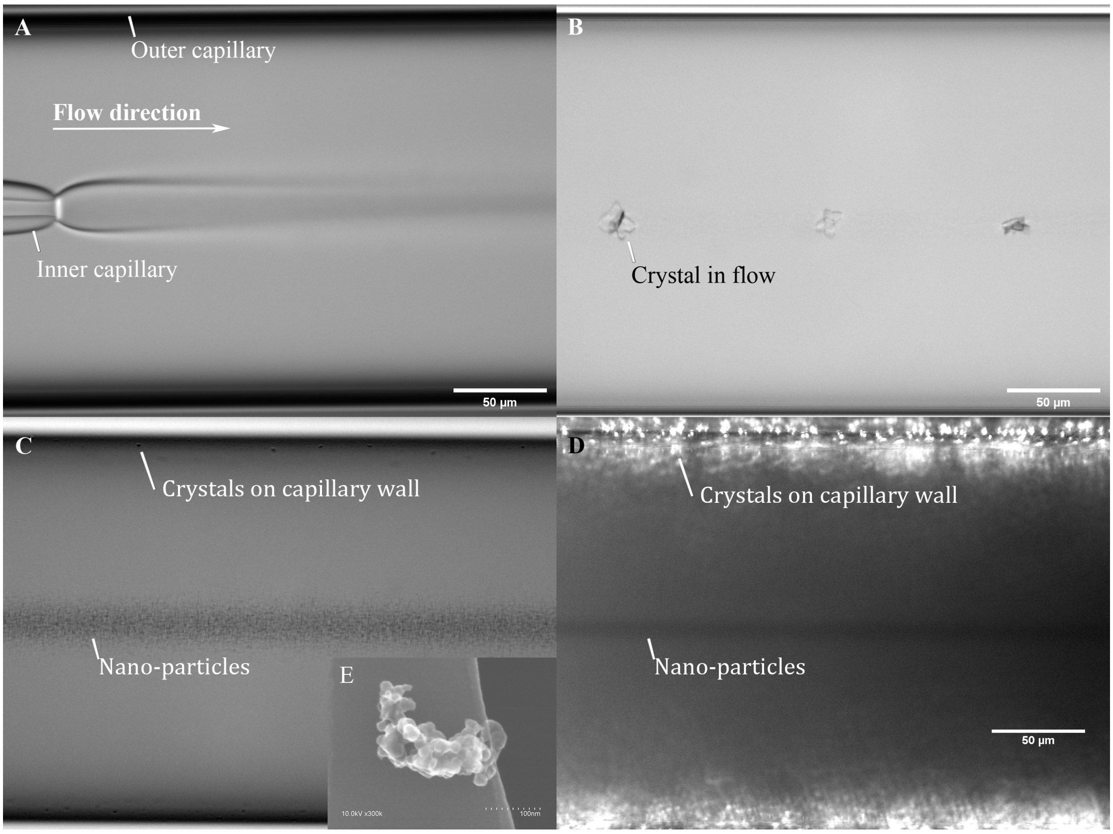

Figure SR1. Microfluidic observation of antisolvent crystallization and precipitation of DBDCS in water-[1,4-dioxane] cosolvent mixture. A: the coaxially aligned capillaries, with the central jet being DBDCS in 1,4-dioxane and the peripheral flow a mixture of water and 1,4-dioxane; B: butterfly-shaped crystals of DBDCS flowing along the capillary center; C: nanoparticles of DBDCS flowing along the capillary center; D: birefringence image under crossed polarizers showing the non-birefringent nanoparticles flowing along the capillary center against the background of the birefringent crystals; E: SEM image of the nanoparticles.